Response to Reviewers

Dear editor and reviewers:

Thank you very much for your letter and the constructive comments concerning our manuscript, now entitled "*Impacts of synoptic circulation types on nocturnal ozone increase in the North China Plain: Meteorological drivers and physical mechanisms*" (Manuscript ID: egusphere-2026-25).

We deeply appreciate the time and effort you have dedicated to reviewing our work. The insightful feedback has been exceedingly valuable in refining our terminology, strengthening our scientific arguments, and improving the overall quality of the paper. We have carefully considered all the comments and revised the manuscript accordingly.

General Update: Please note that to ensure absolute terminological rigor and to perfectly align with the reviewers' excellent suggestions, we have slightly adjusted the title from "...formation mechanisms" to "...physical mechanisms".

Please find below our detailed point-by-point responses to the specific comments as follows:

Reviewers' comments are in black.

Authors' responses are in blue.

Changes in the manuscript are in red.

Your Sincerely,

Liya Fan,

On behalf of the authors

Reviewer #1

Major comments:

1. The authors selected only four stations in Xinxiang City for their study and further identified 197 days during which NOI events occurred simultaneously at all stations as a representative sample. Why do these four stations, which are located relatively close to one another, have more days with non-overlapping NOI events than days with overlapping events? If the NOI is primarily driven by large-scale atmospheric circulation, why did the four sites not experience simultaneous events? This strongly suggests the dominant role of local emissions or mesoscale processes, making the authors' subsequent focus on the analysis of large-scale atmospheric circulation appear to lack a solid foundation.

Response 1: Thanks for reviewer's comments. The ultimate occurrence of NOI is indeed inextricably linked to localized boundary-layer and mesoscale processes. Rather than contradicting our focus on synoptic circulations, this physical reality is the exact theoretical foundation for our specific sampling strategy.

Our detailed rationale is as follows, which we have now clarified in the revised manuscript:

(1) We deliberately selected these four stations for two critical reasons. First, high representativeness: they are all official state-controlled environmental monitoring stations (national network). Collectively, they provide a highly representative spatial footprint of the city's core urban environment. Second, robust data completeness: compared with other regional sub-stations, these four state-controlled stations exhibit the highest data integrity and continuity over our long-term study period, ensuring the robust quality of our observational basis and preventing any single-site measurement bias.

(2) Physical meaning of non-overlapping events (filtering random noise): Local emissions and highly isolated micro-topographic eddies can trigger NOI at individual sites. However, these non-overlapping events represent highly localized, decoupled random noise (e.g., a random emission plume or a strictly localized sub-grid eddy). Analyzing these days would obscure the systematic physical mechanisms we aim to reveal.

(3) Core paradigm (macro-to-micro scale): We strictly selected days with simultaneous NOI events across all four stations not to neglect local boundary-layer physics, but to ensure that the local boundary-layer changes were systematically driven by a unified macro-scale forcing. When

NOI occurs simultaneously across the entire urban footprint, it strongly implies a macro-to-micro scale cascade: a powerful synoptic-scale forcing (e.g., massive subsidence, strong advection) successfully and universally triggered the necessary localized boundary-layer turbulence (e.g., enhanced mechanical wind shear, U^* spikes) across the entire region.

(4) Solidifying the foundation: Our representative sample isolates the events where large-scale atmospheric circulations act as the overarching commanders, while localized boundary layer dynamics act as the executors. Focusing our Lamb-Jenkinson weather classification and mechanistic analysis on this specific subset provides a rigorous foundation for revealing how different synoptic patterns uniquely modulate local boundary layer mechanics to trigger NOI.

This rationale was not sufficiently articulated in the original manuscript, which led to the misunderstanding. We have now explicitly added this justification in the Section 2.3 to clarify the scientific premise of our sampling strategy.

Lines 92-93:

In this study, these four stations were deliberately selected due to their strong spatial representativeness over the urban core and their high data completeness.

Lines 234-242:

It is worth noting that non-overlapping NOI events frequently occur among the different stations, highlighting the inevitable influence of random localized emission noise and uncoordinated micro-environmental fluctuations. To rigorously isolate the overarching synoptic-scale meteorological drivers from these random local chemical/emission noises, this study specifically focused on representative events where NOI occurred simultaneously across all stations. Rather than neglecting local boundary-layer processes, these simultaneous occurrences serve as robust indicators of powerful regional episodes. They demonstrate that the large-scale synoptic forcing was sufficiently intense to synchronize the local boundary-layer dynamics (e.g., vertical wind shear and turbulent mixing) across the entire urban region. This rigorous screening ensures that the localized physical mechanisms evaluated in subsequent sections are systematically driven by macro-weather types, rather than coincidental local perturbations.

2. The authors did not specify whether they used meteorological fields covering the entire day for

Lamb-Jenkinson classification. The fundamental flaw in this approach is that the classification is based on average atmospheric circulation throughout the day or at specific times, whereas NOI is a short-term phenomenon occurring during specific hours at night.

Response 2: Thanks for reviewer's comments. Daytime data is heavily dominated by intense solar radiation and daytime convective boundary layer dynamics, blurs and misrepresents the actual synoptic forcing present during the exact nocturnal hours when the O_3 enhancement is triggered.

To resolve this issue and strictly align the synoptic background with the NOI occurrences, we have discarded the daily average approach and recalculated the Lamb-Jenkinson (L-J) classification using strictly nocturnal meteorological fields.

Furthermore, to ensure the utmost methodological rigor and to completely exclude any potential boundary layer convective perturbations near sunrise, we implemented a seasonally-adjusted nocturnal window based on local sunrise times:

(1) For April to September, where sunrise occurs earlier (after 05:00 LT), we averaged the meteorological fields from 20:00 LT to 05:00 LT the following day.

(2) For October to March, where sunrise occurs later (after 06:00 LT), the nocturnal window was extended from 20:00 LT to 06:00 LT the following day.

Using these nighttime sea level pressure (SLP) fields, we re-ran the L-J classification for all representative NOI days. Consequently, all subsequent analyses, including the frequencies of weather types, meteorological characteristic, and mechanistic discussions, have been comprehensively updated.

Lines 143-146:

To accurately capture the synoptic background driving NOI events and to eliminate daytime boundary layer convective perturbations, the classification was performed using strictly nocturnal SLP fields rather than daily averages. Furthermore, a seasonally-adjusted nocturnal window was applied based on local sunrise times, consistent with the nocturnal time window adopted for NOI.

3. Lines 87–92: If I understand correctly, the author defines an NOI event as a rise in hourly O_3 concentration during the night exceeding 10 μg m^{-3} compared to the previous hour. This definition does not account for the diurnal cycle of O_3 concentrations. Between 00:00 and 06:00, as sunrise approaches and temperatures rise, O_3 concentrations naturally tend to increase. If the diurnal cycle

is not accounted for, a significant portion of the detected so-called NOI events may simply be part of normal daily variations.

Response 3: Thanks for reviewer's comments. We have re-evaluated our identification framework to ensure the diurnal cycle is strictly accounted for, addressing reviewer's concerns through two targeted steps:

(1) Clarifying on the concentration changes of normal nocturnal O_3:

Extensive literatures (He et al., 2022; Zhu et al., 2020; Wang et al., 2025; Nair et al., 2002) establish that in the absence of solar radiation, nocturnal O_3 concentrations normally exhibit a continuous decrease from 20:00 LT until sunrise. This is driven by NO titration and surface dry deposition. The normal, sunlight-driven diurnal rebound of surface O_3 typically does not begin until 06:00–08:00 LT (depending on the season). Therefore, a sudden, short-term spike exceeding 10 μg m^{-3} occurring in the deep night (e.g., between 00:00 and 04:00 LT) is highly anomalous. It is distinctly not a part of the normal daily variation but is primarily driven by physical transport mechanisms (such as downward mixing from the residual layer).

(2) Eliminating of the approaching sunrise interference:

As summer approaches, sunrise occurs earlier (e.g., before 06:00 LT). If the identification window extends to 06:00 LT during these warmer months, there is a genuine risk that the detected O_3 increase might be partially contaminated by early-morning photochemical production rather than purely nighttime dynamic transport. To rigorously eliminate this false-positive threat and completely isolate our analysis from the daytime diurnal cycle, we redefined our NOI identification window using the same seasonally-adjusted strategy mentioned in our response to Comment 2:

For April to September, since sunrise is earlier, we strictly truncated the identification window to 20:00-05:00 LT the following day.

For October to March, the window remained at 20:00-06:00 LT the following day.

Lines 126-129:

Considering the seasonal variation in local sunrise time, we excluded NOI events occurring after 05:00 LT from April to September, when the sunrise occurs relatively early. Since nighttime generally lasts from 20:00 to 06:00 LT the next day, it constitutes a continuous process. Therefore, a day is classified as an NOI day if such events occur from 20:00 to 06:00 LT the next day (excluding April to September, for which the window is 20:00 to 05:00 LT).

4. The grouping of weather types is overly subjective and lacks quantitative justification, resulting in ambiguity regarding the physical significance of the categories. The authors subjectively grouped the 23 weather types generated by the Lamb-Jenkinson method into four major categories: A-type, C-type, S-type, and WNE-type. The rationale for this grouping is stated as being "based on the position of central system and different meteorological elements of each classification", but this has not been quantified or clearly explained in the manuscript.

Response 4: Thanks for reviewer's comments. The original manuscript lacked a rigorous, quantitative explanation for grouping the Lamb-Jenkinson weather types into four major categories (A, C, S, and WNE). The primary objective of this grouping was to reduce dimensionality and extract the overarching physical mechanisms driving NOI, but we realize that the lack of explicit quantitative justification made the process appear subjective.

To rectify this and provide a robust quantitative foundation, we have made our grouping criteria completely transparent, based rigorously on the objective physical properties of the synoptic systems (specifically, SLP anomalies and geostrophic wind vorticity):

(1) Quantitative grouping criteria:

A-type (Anticyclonic group): This category quantitatively lumps all subtypes characterized by strong anticyclonic vorticity and positive SLP anomalies dominating the North China Plain (e.g., Pure A, and hybrid A types like AE, AW). Physically, these are unified by their shared capacity to induce broad regional subsidence.

C-type (Cyclonic group): This lumps subtypes dominated by cyclonic vorticity and negative SLP anomalies (e.g., Pure C, and hybrid C types), unifying them through their shared dynamic triggering of localized convective downdrafts or atmospheric instability.

S-type (Southerly group) & WNE-type (West-North-East group): The directional types were categorized quantitatively based on the dominant azimuth of the geostrophic wind vectors and the strong orientation of the pressure gradient force, representing distinct horizontal advection and shear-induced mixing profiles.

(2) Quantitative verification (new composite analysis & analysis of variance):

To definitively eliminate any ambiguity regarding their distinct physical significance, we conducted two major additions to the revised manuscript:

Composite synoptic patterns (new Fig. 5): We calculated the composite mean fields (SLP and 850 hPa wind vectors) for these four major categories. These composites were calculated strictly using the seasonally-adjusted nocturnal window. The newly added Fig. 5 unequivocally demonstrates that the four groups possess fundamentally distinct synoptic pressure distributions and low-level advection characteristics.

Statistical significance test (Fig. 6 and Table S2): We conducted a One-Way Analysis of Variance (ANOVA) on the nocturnal anomalies of key local meteorological variables (T, RH, WS, PBLH and U^*) across the four groups. As shown in the new Fig. 6 and Table S2, the inter-group differences are highly statistically significant (all $p < 0.01$). This firmly proves that our classification objectively separates fundamentally different boundary layer thermodynamic environments.

Lines 276-282:

Notably, to extract the overarching dynamical mechanisms and reduce the statistical noise of the 20 specific Lamb-Jenkinson weather types, we quantitatively clustered them into four major archetypes: Anticyclonic (A-type), Cyclonic (C-type), Southerly (S-type), and West-North-East (WNE-type). Rather than subjective grouping, this clustering was rigorously based on their shared physical topology: specifically, the polarity of SLP anomalies, geostrophic vorticity, and the primary azimuth of geostrophic wind vectors. The detailed quantitative criteria for each of the four weather types are provided in Text S2. To further validate the physical distinctness of this categorization, composite analysis of the synoptic fields and Analysis of Variance (ANOVA) on localized boundary layer variables were conducted.

Lines 283-296:

To verify that the four grouped weather types possess fundamentally distinct atmospheric backgrounds, we analyzed their composite mean SLP and 850 hPa wind fields (Fig. 5). The spatial distributions unequivocally demonstrate distinct synoptic forcings: A-type is dominated by a strong, uniform high-pressure center over the study region (Fig. 5(a)); C-type is characterized by cyclonic curvature and low-pressure system (Fig. 5(b)); S-type is driven by intense southerly advection between a western low and an eastern high (Fig. 5(c)); and WNE-type features strong northeasterly flows driven by a massive continental high to the northwest (Fig. 5(d)). Furthermore, to statistically

confirm that these different synoptic structures translate into distinctly different local thermodynamic environments, a One-Way ANOVA was performed on the nocturnal anomalies of key meteorological variables (T, RH, WS, PBLH and U^*) across the four groups. The resulting statistical distributions and data spreads are visually compared in Fig. 6, while the precise quantitative parameters and significance test results are detailed in Table S2. To strictly isolate the meteorological perturbations driven by synoptic systems and to eliminate the influence of seasonal and interannual backgrounds, the nocturnal anomalies (Δ) for key meteorological variables were calculated as the difference between the NOI days' specific nocturnal average and the corresponding monthly nocturnal mean. The results show that the inter-group differences are highly statistically significant (all $p < 0.01$), definitively proving that our quantitative classification objectively separates fundamentally different boundary layer environments.

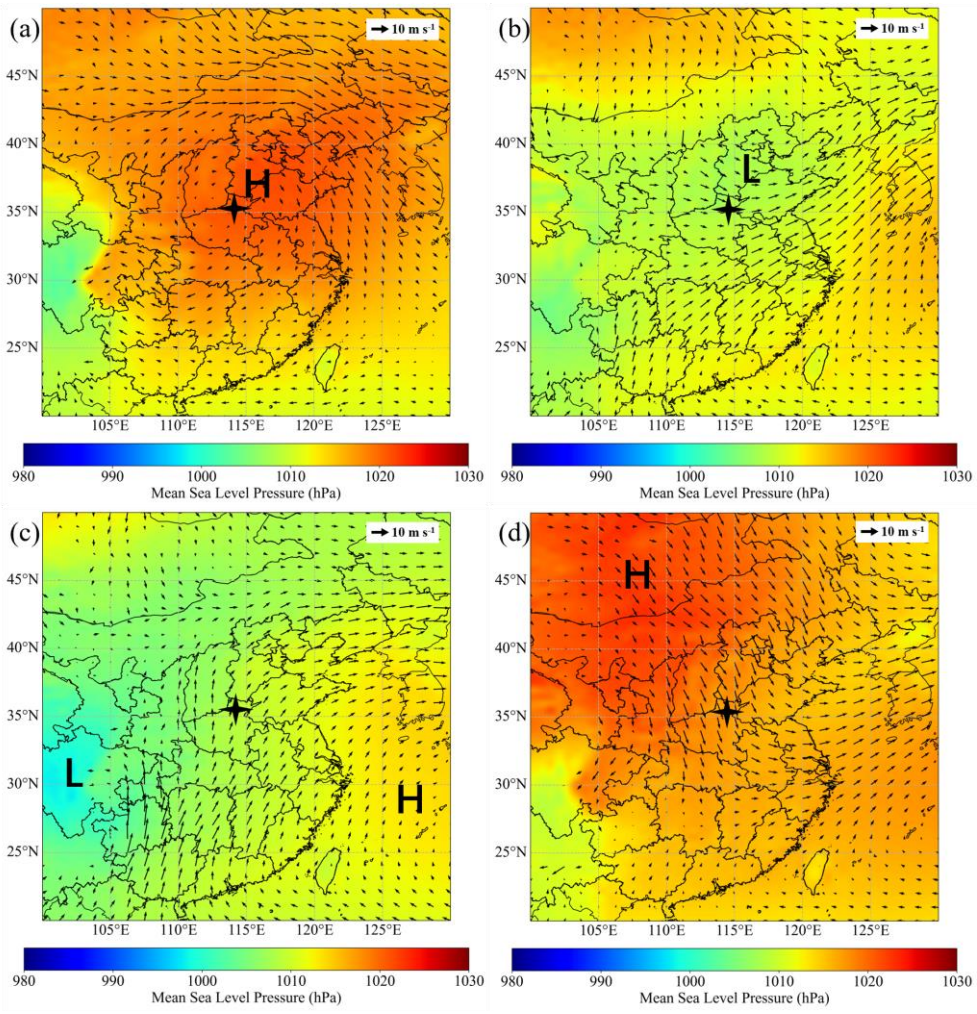


Figure 5: Spatial distribution of composite mean SLP and 850 hPa wind fields under different weather categories: (a) A-type, (b) C-type, (c) S-type, (d) WNE-type (asterisk indicates the location of Xinxiang; "H" and "L" stand

for high-pressure and low-pressure, respectively).

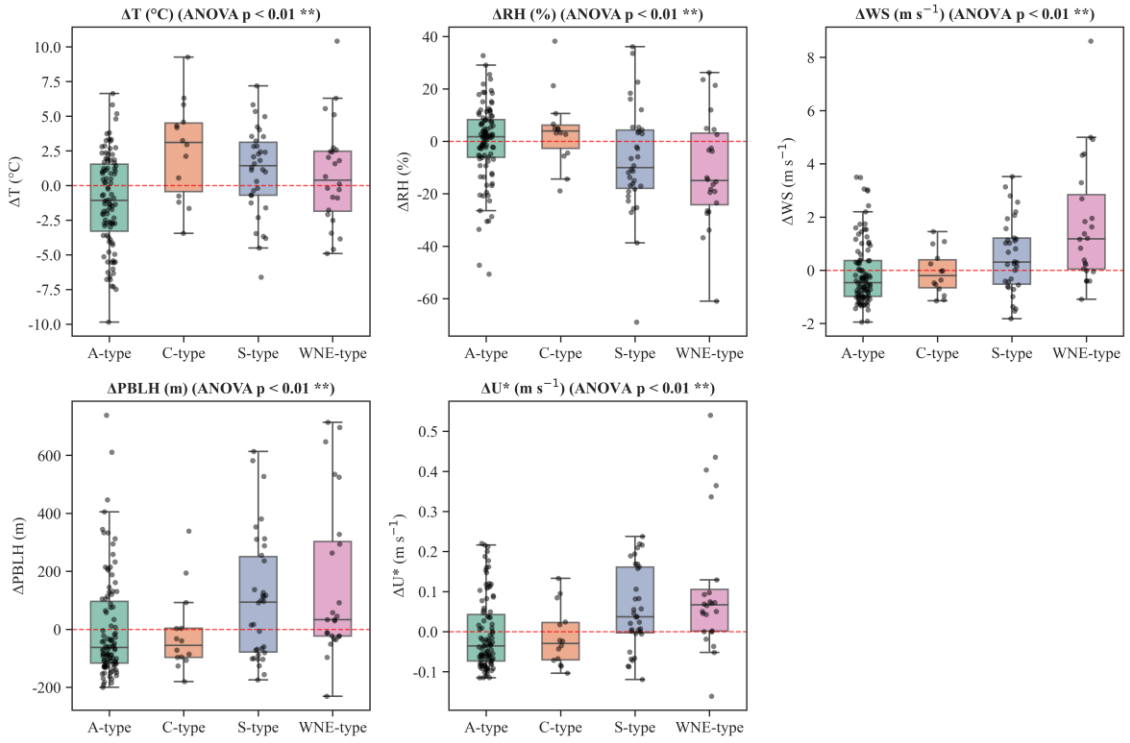


Figure 6: One-Way ANOVA results for key meteorological variables (T, RH, WS, PBLH and U^*) of different synoptic categories. In each boxplot, the central black solid line indicates the median. The horizontal red dashed line denotes the zero-anomaly reference.

Table S2. Statistical summary of nocturnal meteorological anomalies and ANOVA results under the four weather types.

Variable	A-type	C-type	S-type	WNE-type	p-value
ΔT (°C)	-1.07 ± 3.41	2.60 ± 3.54	1.06 ± 3.18	0.77 ± 3.70	$< 0.01^{**}$
ΔRH (%)	-0.31 ± 14.82	4.08 ± 14.00	-7.12 ± 20.46	-11.15 ± 20.72	$< 0.01^{**}$
ΔWS (m s^{-1})	-0.10 ± 1.21	-0.08 ± 0.83	0.54 ± 1.39	1.74 ± 2.32	$< 0.01^{**}$
ΔPBLH (m)	3.56 ± 178.15	-14.44 ± 139.19	102.41 ± 216.82	156.22 ± 274.82	$< 0.01^{**}$
ΔU^* (m s^{-1})	-0.01 ± 0.09	-0.01 ± 0.07	0.06 ± 0.10	0.11 ± 0.17	$< 0.01^{**}$

Note: Data are presented as Mean ± Standard Deviation. The anomalies (Δ) were calculated relative to their respective monthly nocturnal means. The p-values are derived from One-Way ANOVA tests indicating statistical significance under the four weather types.

Text S2: Quantitative grouping criteria.

(1) A-type (Anticyclonic group): This category quantitatively lumps all subtypes characterized

by strong anticyclonic vorticity and positive SLP anomalies dominating the North China Plain (e.g., Pure A, and hybrid A types like AE, AW). Physically, these are unified by their shared capacity to induce broad regional subsidence.

(2) C-type (Cyclonic group): This lumps subtypes dominated by cyclonic vorticity and negative SLP anomalies (e.g., Pure C, and hybrid C types), unifying them through their shared dynamic triggering of localized convective downdrafts or atmospheric instability.

(3) S-type (Southerly group) & WNE-type (West-North-East group): The directional types were categorized quantitatively based on the dominant azimuth of the geostrophic wind vectors and the strong orientation of the pressure gradient force, representing distinct horizontal advection and shear-induced mixing profiles.

5. The logic of the entire Section 3.3 is inverted. Rather than analyzing how the specific meteorological conditions of each weather type led to NOI, the author devotes a significant amount of space to explaining how the meteorological conditions of each type contribute to the maintenance of atmospheric circulation. Of greater interest is which local meteorological variables (such as temperature, wind, and boundary layer height) directly drive the formation of NOI within the context of already classified atmospheric circulation.

Response 5: Thanks for reviewer's comments. The original Section 3.3 mistakenly focused on the climatological maintenance of the synoptic systems across different seasons, rather than explicitly elucidating the local meteorological drivers of NOI.

To correct this fundamental flaw, we have completely rewritten Section 3.3. We removed the extensive discussions on seasonal climate maintenance. We redirected the entire focus toward analyzing: how the specific local meteorological variables (temperature, wind, relative humidity, and boundary layer height) directly drive the thermodynamic and kinematic environment for NOI under the classified circulations.

To provide robust, quantitative evidence, we integrated the composite synoptic maps (Figs. 5 and 7) with the rigorously calculated nocturnal anomalies of local variables (Fig. 6 and Table S2). The revised Section 3.3 is presented below:

Lines 307-367:

3.3 Meteorological characteristics of primary weather types

As established in Section 3.1, the vast majority of NOI events in Xinxiang occur during the LN period. During this phase, the nocturnal boundary layer is characterized by a fully established surface inversion, creating a highly stable thermodynamic environment. To trigger downward O_3 transport under such extreme stability, localized residual turbulence is entirely insufficient. Instead, it requires massive, active mechanical forcing capable of physically breaking the inversion layer. Because such powerful mechanical triggers are fundamentally governed by macro-scale weather systems, identifying the specific synoptic circulations is the critical next step to unravel the forcing mechanisms behind these NOI events.

It should be noted that while seasonal variations significantly influence the daytime photochemical generation and absolute background concentrations of O_3, the nocturnal occurrence of NOI is predominantly driven by physical transport. As validated by the seasonal comparison (Fig. S6 and Text S3), while the absolute intensity of meteorological variables naturally fluctuates across seasons, the fundamental dynamical frameworks for a given weather type (e.g., the general orientation of horizontal pressure gradients and patterns of vertical motions) maintain functionally comparable mechanical triggers. Therefore, rather than focusing on seasonal background variations, our study focuses on elucidating these primary, synoptically-driven local meteorological drivers that trigger NOI.

The representative NOI days in Xinxiang were classified into four weather types (A-type, C-type, S-type, and WNE-type), with each exhibiting distinct meteorological features. Fig. 7 illustrates the spatial distributions of 850 hPa wind fields under four weather types. Under A-type, Xinxiang was located near a high-pressure center, with an outward-rotating wind field at 850 hPa (Figs. 5(a) and 7(a)), indicating the presence of an anticyclonic high-pressure system. Driven by this synoptic forcing, Xinxiang experienced extremely calm conditions. As explicitly demonstrated by the nocturnal anomalies in Fig. 6 and Table S2, A-type was characterized by negative anomalies in wind speed (mean: $\Delta WS = -0.10$ m s^{-1}) and friction velocity (mean: $\Delta U^* = -0.01$ m s^{-1}), alongside a strongly constrained boundary layer (mean: $\Delta PBLH = 3.56$ m, representing negligible expansion). This indicates that the overriding high-pressure system creates a highly stable environment. The explicit intrusion process of O_3 under this subsidence will be further verified in Section 3.4.

Under C-type, Xinxiang was dominated by low-pressure systems (Fig. 5(b)). At 850 hPa, a strong airflow originating near the coastal region of Guangxi Province moved continuously

northeastward (Fig. 7(b)). This airflow not only moved at a high speed, but also likely carried substantial moisture, significantly enhancing atmospheric instability in its trajectory and surrounding regions (including Xinxiang), intensifying convective activity, and increasing the risk of heavy rainfall. Combined with the water vapor flux and divergence fields at 850 hPa, we find that the intense southwest warm-wet moisture transport belt under C-type is extremely prominent. Significant moisture convergence is observed along the entire path of this belt (including Xinxiang) (Fig. S7). Notably, the local meteorological anomalies perfectly capture this advection, with C-type uniquely coinciding with distinct positive anomalies in temperature (mean: $\Delta T = 2.60$ °C) and the highest relative humidity anomaly among all weather types (mean: $\Delta RH = 4.08\%$). This localized warm and highly humid environment, dynamically coupled with a cyclonic low-pressure background, significantly amplifies atmospheric thermodynamic instability, highly favoring the development of regional convection and precipitation. Consequently, rather than uniform large-scale subsidence, NOI under C-type is primarily triggered by convective downdrafts and the subsequent development of cold pools.

S-type represents a dynamic environment driven by distinct horizontal advection. Under S-type, Xinxiang was situated in a tight pressure gradient, typically between a western low and an eastern high (Figs. 5(c) and 7(c)). Driven by this synoptic setup, continuous southerly geostrophic winds prevailed over the region. As detailed in Table S2, S-type produced significant positive anomalies in local wind speed (mean: $\Delta WS = 0.54$ m s^{-1}) and friction velocity (mean: $\Delta U^* = 0.06$ m s^{-1}). These specific values rigorously demonstrate that beyond facilitating regional horizontal transport (which will be explicitly traced in Section 3.4.1), the southerly advection directly generates substantial localized mechanical turbulence at the surface, physically lifting the nocturnal boundary layer (mean: $\Delta PBLH = 102.41$ m). This localized mechanical shear serves as the direct trigger for breaking nocturnal stability, subsequently entraining O_3-rich air from the elevated residual layer down to the surface and triggering NOI events.

Although Xinxiang often featured a massive continental high-pressure system (e.g., the Siberian High) to the northwest under WNE-type (Fig. 5(d)), their local dynamics are fundamentally different from the pure subsidence of A-type. At 850 hPa, the region was obviously influenced by a northwestern airflow (Fig. 7(d)), consistent with the geostrophic wind characteristics of WNE-type. Unlike A-type, where the study area sits calmly at the high-pressure

center, under WNE-type, Xinxiang was located at the densely packed periphery of the advancing high. Consequently, the macroscopic forcing shifts to intense horizontal pressure gradients (Figs. 5(d) and 7(d)). This kinematic distinction is perfectly captured by the localized surface anomalies (Table S2). WNE-type exhibited the most extreme positive anomalies among all categories, with local wind speed (mean: ΔWS = 1.74 m s^{-1}) and friction velocity (mean: ΔU^* = 0.11 m s^{-1}) far exceeding other types. Driven by this intense horizontal advection and wind shear, the nocturnal boundary layer experienced massive mechanical lifting (mean: $\Delta PBLH$ = 156.22 m). Furthermore, this intense mechanical mixing effectively breaks the nocturnal surface inversion, bringing slightly warmer air from aloft downward (detailed mechanism analysis is presented in Section 3.4.2). This vigorous downward mixing of the elevated residual layer shares conceptual similarities with the nocturnal fumigation-like processes documented in other literature (Wu et al., 2023; He et al., 2022), which also explains the observed positive temperature anomaly (mean: ΔT = 0.77 °C). Therefore, despite the high-pressure background, it is this extraordinarily strong localized shear and turbulent mixing, that serves as the primary mechanical driver forcing O_3 downward to the surface during WNE-type. Combined with rapid dispersion of local NO emissions under high winds that greatly mitigates nighttime titration, vigorous vertical entrainment counteracts both horizontal diffusion and titration loss of O_3, and ultimately causes a net O_3 surge.

6. In the analysis of NOI formation mechanisms, it is unreasonable to study the mechanisms of NOI occurring in different seasons together. For example, the S-type events in spring and those in autumn have vastly different precursor substances and meteorological conditions, which naturally leads to differences in the formation mechanisms of NOI.

Response 6: Thanks for reviewer's comments. The baseline meteorological conditions and chemical precursor substances (e.g., VOCs and NO_x) indeed vary profoundly across seasons. Under normal circumstances (especially regarding daytime photochemical O_3 production), analyzing different seasons together would be unreasonable.

We carefully re-evaluated our unified approach. We ultimately retained the cross-seasonal grouping based on the following specific physical and statistical considerations, which we have now better clarified in the manuscript:

(1) Isolating nocturnal physical transport from chemical production: Because our study

specifically isolates the nocturnal sudden spikes (NOI), which is a period when photochemical production ceases and rapid physical transport (e.g., downward intrusion from the residual layer) dominates the variance. We found that the overarching mechanical triggers operate somewhat independently of the seasonal chemical baselines. For instance, the mechanical shear required to break the nocturnal inversion relies on the synoptic dynamic framework. This physical mechanism remains fundamentally consistent across seasons, even though the absolute baseline O_3 concentrations and precursor emissions differ.

(2) Balancing seasonal stratification with statistical robustness: We attempted to stratify the mechanisms by season, but we encountered a practical limitation: subdividing the unified major categories into four distinct seasons severely fragmented our sample size of 171 NOI days. This fragmentation significantly weakened the statistical power of our boundary-layer anomaly tests (e.g., the ANOVA in Table S2), making it difficult to extract robust, overarching synoptic-scale signals without being overwhelmed by localized statistical noise.

(3) Empirical verification of dynamical consistency (Fig. S6): To ensure that our unified grouping did not obscure crucial seasonal differences, we conducted an additional seasonal stratification analysis specifically for the S-type (Fig. S6). The results confirmed that the underlying dynamical frameworks are functionally comparable among seasons:

Horizontal synoptic forcing: As shown in Figs. S6(a) and (b), the SLP gradient (which rigorously defines the Lamb-Jenkinson weather typing) drives a robust, seasonally consistent southerly airflow through the study region in both spring and autumn. The fundamental spatial pattern of this forcing remains unchanged.

Vertical structure of motion: Vertically, Figs. S6(c) and (d) reveal a consistent pattern of vertical motion. In both seasons, the region is dominated by prominent upward velocities.

Lines 314-320:

It should be noted that while seasonal variations significantly influence the daytime photochemical generation and absolute background concentrations of O_3, the nocturnal occurrence of NOI is predominantly driven by physical transport. As validated by the seasonal comparison (Fig. S6 and Text S3), while the absolute intensity of meteorological variables naturally fluctuates across seasons, the fundamental dynamical frameworks for a given weather type (e.g., the general orientation of horizontal pressure gradients and patterns of vertical motions) maintain functionally

comparable mechanical triggers. Therefore, rather than focusing on seasonal background variations, our study focuses on elucidating these primary, synoptically-driven local meteorological drivers that trigger NOI.

Text S3: Cross-seasonal dynamical consistency of weather types.

To demonstrate that the dynamical mechanisms driving NOI under a specific synoptic classification remain functionally consistent across different seasons, a seasonal stratification analysis was conducted for S-type (Fig. S6).

(1) Horizontal synoptic forcing: As shown in Figs. S6(a) and (b), both spring and autumn S-type are driven by a virtually identical synoptic pressure gradient: lower SLP to the west and a prominent high-pressure system to the east. This forces a robust, seasonally-consistent southerly airflow directly through the study region. The spatial pattern of forcing is fundamentally unchanged.

(2) Vertical structure of motion: Vertically, Figs. S6(c) and (d) confirm a highly consistent structure of vertical motion. In both spring and autumn, the region around Xinxiang is dominated by a prominent upward motion ($\omega < 0$).

(3) Consistency check: The only discernible difference is in the intensity. This verification definitively proves that the overarching physical triggers are functionally comparable across seasons under S-type.

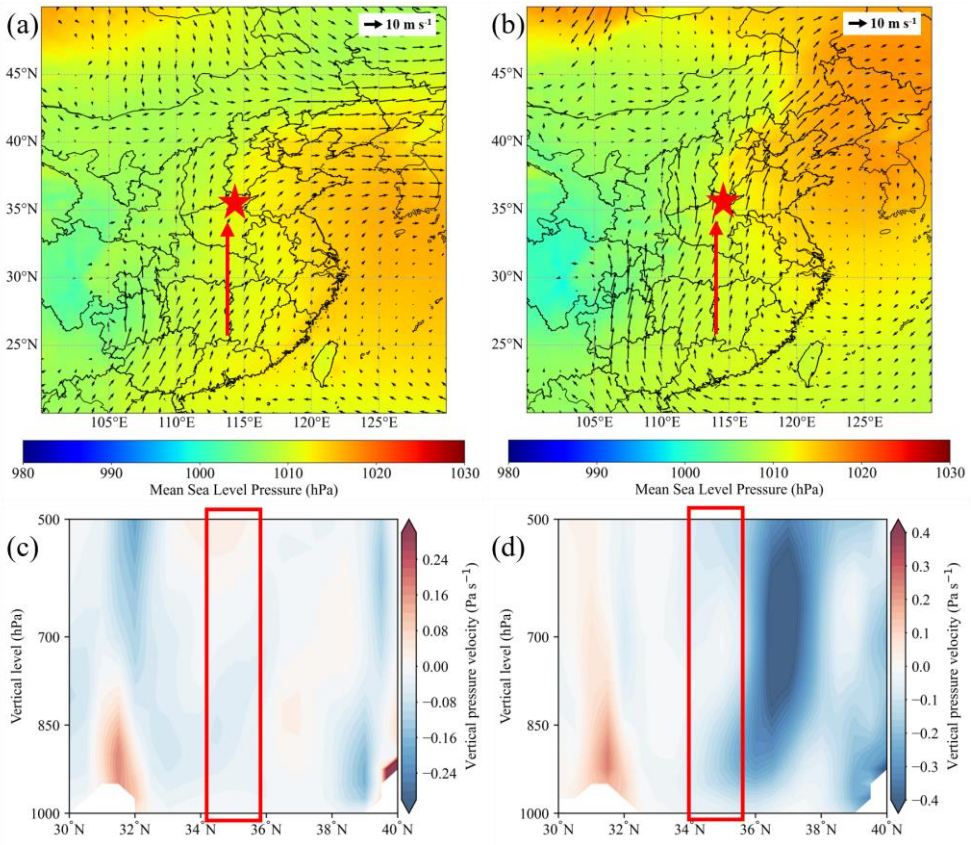


Figure S6: During spring ((a) and (c)) and autumn ((b) and (d)), spatial distribution of composite mean SLP and 850 hPa wind fields ((a) and (b)), and vertical profiles of pressure velocity ((c) and (d)) under S-type (asterisk indicates the location of Xinxiang; red rectangles indicate the region of Xinxiang). In terms of vertical pressure velocity, negative values correspond to upward motion, while positive values indicate subsidence.

Specific comments:

1. The content within the parentheses in the caption of Figure S5 is not specified.

Response 1: Thanks for reviewer's comments. The numbers in parentheses are indeed 4-digit binary codes used to indicate the occurrence status of NOI events across the four specific stations.

The four digits correspond to the occurrence of NOI in DX, XY, DY, and KF stations, respectively. A value of 1 denotes the occurrence of an NOI event at that specific station, while "0" denotes non-occurrence. For instance, (1111) indicates that the NOI event was observed simultaneously at all four stations (the cooccurrence of all four sets), whereas (1000) indicates that the event was observed only at the DX station.

We have now added this detailed explanation to the caption of Figure S5 (revised Figure 3) to

eliminate any ambiguity for the readers.

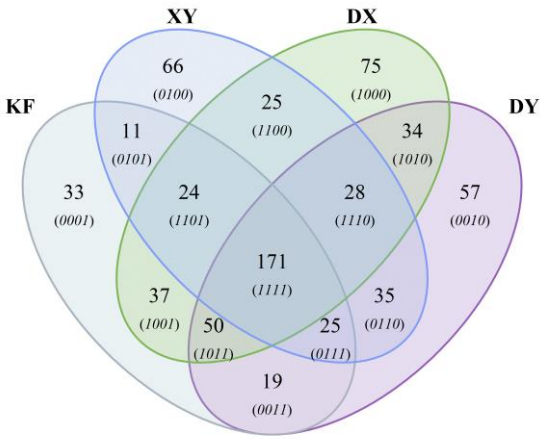


Figure 3: Overlapping occurrences of NOI days at national monitoring stations in Xinxiang, 2021-2023. The four-digit binary codes in parentheses indicate the specific occurrence status of NOI events across the four stations (in the order of DX, XY, DY, and KF). A digit of 1 represents the occurrence of the event, and 0 represents non-occurrence (e.g., (1111) denotes cooccurrence at all four stations, while (1000) denotes occurrence only at the DX station).

2. The reference to Figure 1 on line 160 does not support the explanation of the preceding sentence; please correct this. After the correction, the entire content of Section 3.1.2 is cited from the Appendix; consider incorporating some of this content from the Appendix into the main text.

Response 2: Thanks for reviewer's comments. We have revised relevant txt in manuscript.

(1) Clarification on Figure 1:

In Figure 1, the dotted line labeled "overlap" represents the "representative NOI days" (i.e., the 171 days when NOI occurred simultaneously at all four stations). As shown by this "overlap" line in Figure 1, its monthly variation trend (e.g., peaks in March and September, and dips in January and December) is consistent with the variations observed at the individual stations. We have revised the manuscript to state this connection, ensuring the text is fully supported by Figure 1.

(2) Incorporating appendix content into the main text:

Section 3.1.2 previously relied too heavily on the supplementary information. To improve the coherence and substance of the main text, we have moved the O_3 diurnal variations analysis (previously Figure S4) directly into the main text as the new Figure 2. We also moved the Venn diagram, previously Figure S5, into the main text as Figure 3.

Lines 242-244:

Furthermore, the monthly variation of these representative regional events (indicated by the "overlap" dotted line in Fig. 1) consistently matches the seasonal trends observed at individual stations (e.g., distinct peaks in March and September, and dips in January and December).

3. Lines 190–195: The authors merely state facts (e.g., Type A events occur more frequently in autumn) without linking them to the subsequent analysis of NOI mechanisms. How does this information contribute to understanding the causes of NOI?

Response 3: Thanks for reviewer's comments. Merely stating descriptive seasonal statistics of weather types without linking them to the fundamental physical mechanisms significantly weakened the narrative flow and distracted from the core focus of the paper.

Upon deep reflection on this comment, and to address reviewer's related concern regarding seasonal mechanism analysis in Comment 6, we realized that these purely descriptive seasonal breakdowns did not actively contribute to understanding the dynamic causes of NOI. As we detailed in our response to Comment 6, the overarching mechanical triggers (e.g., macroscopic wind shear and subsidence) of a given weather type remain functionally consistent across different seasons.

Therefore, to drastically improve the analytical clarity and maintain a strict focus on the physical drivers, we have completely deleted this descriptive paragraph regarding the seasonal frequencies of weather types in the revised manuscript. Instead, we have restructured the entire mechanism section to focus strictly on how the synoptic circulations govern the localized boundary-layer dynamics, eliminating the descriptive distractions. The revised Section 3.3 can be found Lines 307-367.

4. Lines 205–210 and Table S2: The analysis of meteorological conditions for each weather type here lists only averages but does not include any significance tests.

Response 4: Thanks for reviewer's comments. To address this and enhance the statistical robustness of our study, we have made the following major revisions:

(1) Removing the previous unverified averages: We have deleted the previous seasonal average analysis that lacked statistical support.

(2) Introducing rigorous ANOVA tests: We conducted a One-Way Analysis of Variance

(ANOVA) to rigorously test whether the differences in the nocturnal meteorological anomalies (T, RH, WS, PBLH and U^*) across the four weather types are statistically significant.

(3) Updating Figures and Tables: The results of the significance tests are now comprehensively visualized in the newly added Figure 6 (which displays the distributions and ANOVA results) and thoroughly detailed in the completely revised Table S2 (which now includes the statistical summary and corresponding p-values).

As shown in the updated Figure 6 and Table S2, the ANOVA tests confirm that the micro-meteorological responses to the different synoptic forcings are indeed statistically significant (typically $p < 0.01$), thereby providing a solid, quantitative foundation for our dynamical mechanism analysis in Section 3.3.

Lines 288-296:

Furthermore, to statistically confirm that these different synoptic structures translate into distinctly different local thermodynamic environments, a One-Way ANOVA was performed on the nocturnal anomalies of key meteorological variables (T, RH, WS, PBLH and U^*) across the four groups. The resulting statistical distributions and data spreads are visually compared in Fig. 6, while the precise quantitative parameters and significance test results are detailed in Table S2. To strictly isolate the meteorological perturbations driven by synoptic systems and to eliminate the influence of seasonal and interannual backgrounds, the nocturnal anomalies (Δ) for key meteorological variables were calculated as the difference between the NOI days' specific nocturnal average and the corresponding monthly nocturnal mean. The results show that the inter-group differences are highly statistically significant (all $p < 0.01$), definitively proving that our quantitative classification objectively separates fundamentally different boundary layer environments.

5. Line 220: The authors infer that the 850 hPa wind field "likely carried substantial moisture" based solely on the wind field itself. We recommend providing more direct evidence, such as calculating and presenting the 850 hPa water vapor flux and its divergence.

Response 5: Thanks for reviewer's comments. We have quantitatively calculated the 850 hPa water vapor flux and its divergence to provide direct evidence. The results are now presented in the newly added Figure S7.

As demonstrated in Figure S7, under C-type conditions, there is a prominent and intense southwesterly moisture transport belt (highlighted by the red box). Furthermore, significant moisture convergence is clearly observed along the entire path of this belt, directly encompassing the Xinxiang region (green box). This direct thermodynamic evidence robustly corroborates our previous inference, confirming that this airflow carries substantial moisture conducive to regional convection.

We have incorporated these findings into the revised manuscript to strengthen the mechanistic explanation for C-type events.

Lines 333-336:

Combined with the water vapor flux and divergence fields at 850 hPa, we find that the intense southwest warm-wet moisture transport belt under C-type is extremely prominent. Significant moisture convergence is observed along the entire path of this belt (including Xinxiang) (Fig. S7).

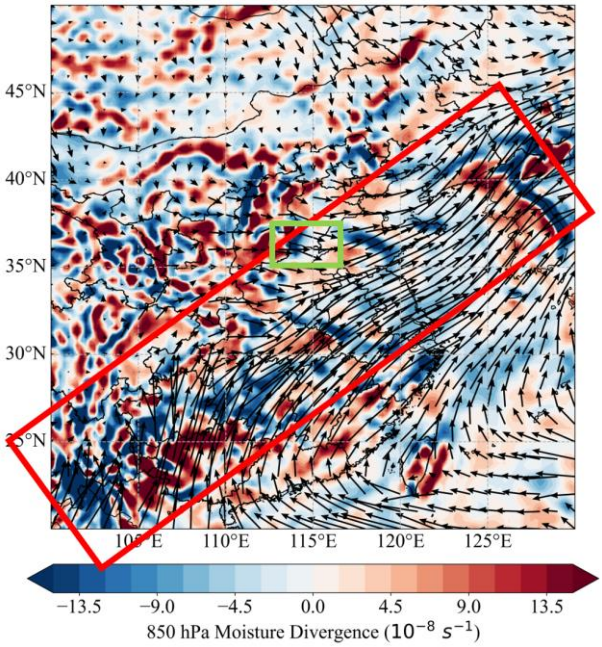


Figure S7: 850 hPa water vapor flux and divergence fields under C-type (the red box denotes the moisture transport path, corresponding to Fig. 5(b); the green box marks the Xinxiang region).

Reviewer #2

General comments:

1. Scientific Significance of NOI: The introduction does not sufficiently justify the atmospheric importance of NOI episodes. A nighttime increase of 10 μg m^{-3} may be numerically detectable, but its impact on overall air quality or subsequent daytime peaks is not clearly established, particularly when background levels are low. The authors should better articulate the scientific or environmental relevance of studying these specific increments.

Response 1: Thanks for reviewer's comments. We have expanded the introduction to justify the scientific and environmental significance of NOI episodes beyond their numerical definitions. Specifically, we have emphasized two critical atmospheric impacts:

(1) Elevation of the next-day baseline:

Although the absolute nighttime O_3 concentration is generally lower than the daytime peak, NOI events induced by horizontal or vertical transport can markedly elevate the surface O_3 baseline on the following morning. A higher morning baseline concentration can lead to higher likelihood of O_3 exceedance.

(2) Altering nighttime atmospheric oxidative capacity (AOC):

Even under low background levels, sudden increments of nighttime O_3 actively drive nocturnal chemistry. Enhanced O_3 reacts with NO_2 to produce nitrate radicals (NO_3) and dinitrogen pentoxide (N_2O_5), which are vital precursors for secondary organic aerosols (SOA) and particulate nitrate. Thus, NOI is deeply coupled with nighttime $PM_{2.5}$ pollution.

We have integrated these mechanistic justifications into the third paragraph of the Introduction to explicitly establish the scientific relevance of studying these increments.

Lines 44-55:

Previously, nocturnal O_3 was often overlooked owing to its low concentrations. Although a quantitative threshold of a 10 μg m^{-3} hourly increase may appear modest during a clean night, the scientific and environmental significance of NOI episodes extends far beyond simple numerical detection. First, NOI events can occasionally result in a rapid surge in nighttime O_3 levels surpassing 160 μg m^{-3} (Wang et al., 2023b; Zhu et al., 2024), directly posing nocturnal threats to human health and plant stomatal uptake (Chowdhury et al., 2022; Hoshika et al., 2019). More

critically, even when absolute concentrations remain moderate, the horizontal or vertical transport of O_3-rich air that typically triggers NOI significantly elevates the surface O_3 baseline for the following morning. This higher initial baseline accelerates daytime accumulation, effectively exacerbating subsequent daytime photochemical smog (Wang et al., 2025). Furthermore, unexpected nighttime O_3 increments fundamentally alter the nocturnal atmospheric oxidative capacity (AOC). The enhanced O_3 facilitates dark reactions with nitrogen dioxide (NO_2) to generate nitrate radicals (NO_3) and dinitrogen pentoxide (N_2O_5), critical precursors for particulate nitrate and secondary organic aerosols (SOA), thereby linking NOI directly to regional fine particulate matter ($PM_{2.5}$) pollution (Wang et al., 2023a).

2. The NOI classification in Section 2.2 appears somewhat arbitrary. The unequal duration of the defined periods makes frequency comparisons statistically difficult. Furthermore, the transition from a time-based categorization to a weather-type categorization is abrupt and creates a disjointed narrative. The authors should harmonize these approaches or more clearly explain how the two frameworks intersect.

Response 2: Thanks for reviewer's comments. We have made the following revisions:

(1) Renaming the time-based categories:

We have abandoned the "Type A/B/C" nomenclature for occurrence times. They are now descriptively renamed as: Early-night NOI (EN): 20:00-23:00 LT (4 hour); Late-night NOI (LN): 00:00-06:00 LT (7 hour); Whole-night NOI (WN): Both EN and LN periods.

(2) Justification of unequal duration and arbitrary cutoffs:

The division between 23:00 and 00:00 is not mathematically arbitrary but physically rooted in the evolution of the nocturnal boundary layer. The EN period represents the transition phase where residual daytime turbulence may still exist. The LN period represents the deep-night phase where the surface inversion is fully established and highly stable. Even if we normalize the occurrences by the duration of the respective windows (yielding hourly occurrence rates), LN (9.93% per hour, 69.53% / 7 hour = 9.93%) still vastly outnumbers EN (5.42% per hour, 21.69% / 4 hour = 5.42%), proving that post-midnight events genuinely dominate.

(3) Harmonizing the narrative (bridging time and weather):

To eliminate the abrupt transition, we have added a bridging paragraph. We explicitly explain

that the time-based framework (identifying that most NOI occurs during the highly stable LN period) dictates the thermodynamic prerequisite. Breaking this late-night stability requires massive mechanical forcing, which directly motivates the second framework: the synoptic weather typing (identifying which specific weather systems provide this forcing).

We have revised Section 2.2 and the transition paragraphs in Section 3 to reflect these changes, thereby harmonizing the two approaches into a single, cohesive physical narrative.

Lines 132-137:

Rather than using arbitrary mathematical intervals, the specific timeframes for these types were chosen to perfectly align with the distinct physical evolution phases of the nocturnal boundary layer: (1) Early-night NOI (EN): The event occurs only between 20:00 and 23:00 LT, corresponding to the transitional boundary layer phase; (2) Late-night NOI (LN): The event occurs only between 00:00 and 06:00 LT, corresponding to the highly stable surface inversion phase; (3) Whole-night NOI (WN): The event occurs across both periods, persisting continuously through the night.

Lines 308-313:

As established in Section 3.1, the vast majority of NOI events in Xinxiang occur during the LN period. During this phase, the nocturnal boundary layer is characterized by a fully established surface inversion, creating a highly stable thermodynamic environment. To trigger downward O_3 transport under such extreme stability, localized residual turbulence is entirely insufficient. Instead, it requires massive, active mechanical forcing capable of physically breaking the inversion layer. Because such powerful mechanical triggers are fundamentally governed by macro-scale weather systems, identifying the specific synoptic circulations is the critical next step to unravel the forcing mechanisms behind these NOI events.

3. Station Typology: A critical omission is the lack of information regarding monitoring site classification (e.g., urban, rural, industrial). Since ozone concentrations are heavily influenced by local NO titration and precursor availability, the interpretation of NOI events is incomplete without considering the specific typology of the stations used in the study.

Response 3: Thanks for reviewer's comments. To clarify, the four stations (KF, DY, XY, and DX) selected for this study are all national air quality monitoring stations, specifically classified as urban

background/evaluation sites. They are primarily located within the urban area of Xinxiang, carefully sited to avoid direct micro-scale emission sources (e.g., immediate proximity to industrial facilities or major highway traffic).

Because these four stations share a highly consistent urban typology, they experience comparable regional chemical environments and baseline NO titration levels. This homogeneity in the local chemical sink is precisely what allows us to minimize localized chemical biases. Consequently, when concurrent NOI events are observed across these stations, we can confidently attribute them to overarching regional meteorological and dynamical drivers (as analyzed in Section 3), rather than localized chemical perturbations.

We have added this vital information regarding the monitoring site classification to Section 2.1 to provide a complete context for our interpretation of NOI events.

Lines 91-99:

It is important to note that all four stations are officially classified as urban evaluation sites located within the urban areas of Xinxiang. In this study, these four stations were deliberately selected due to their strong spatial representativeness over the urban core and their high data completeness. Because these stations share a consistent urban typology, they experience highly comparable baseline chemical environments (e.g., similar baseline nitrogen monoxide (NO) titration sinks and anthropogenic precursor availability). This spatial consistency is a crucial methodological design: it effectively minimizes random micro-scale chemical biases and isolated emission noise. By strictly controlling for these localized chemical heterogeneities, we ensure that the concurrent NOI events captured by this network genuinely reflect the overarching regional synoptic forcing and its subsequent, synchronized mechanical disruption of the local boundary layer, rather than random chemical artifacts.

4. Vertical Transport Analysis: The back-trajectory analysis is currently limited to the surface level. Given that the downward transport of ozone from the residual layer or upper troposphere is a well-documented driver of ozone increases, it is essential to include trajectories at higher altitudes to capture the full transport dynamics.

Response 4: Thanks for reviewer's comments. Initially, we considered running backward trajectories arriving at higher altitudes (e.g., 500m or 1000m). However, from a Lagrangian

transport perspective, an upper-level arriving trajectory only proves that air masses reached the upper boundary layer, but does not prove that those specific air masses subsequently intruded into the surface layer where the NOI was observed.

Therefore, to provide the most direct evidence of downward intrusion, we utilized a more robust approach: we extracted the 3D altitude-time cross-sections and pressure profiles of the trajectories arriving at the surface. This allows us to trace whether the surface-arriving air masses physically originated from the high-altitude residual layer over the preceding 48 hours.

As shown in the newly added 3D trajectory profiles (Figure S8 in the revised manuscript, corresponding to the right and left columns of the newly uploaded figure), the results provide spectacular Lagrangian evidence of massive subsidence:

(1) Under A-type, the primary clusters originated from ~800 hPa and ~900 hPa (approx. 1000-2000 m altitude) before continuously subsiding to the surface.

(2) Under C-type, an extremely prominent cluster rapidly subsided from the free troposphere (~700 hPa, >2000 m).

(3) Similar distinct subsiding pathways from the upper residual layer (~800-880 hPa) were observed under S-type and WNE-type.

This 3D Lagrangian evidence of synoptic-scale downward transport perfectly complements our local vertical mixing analysis (detailed in Section 3.4.2). Together, they form a complete 3D transport mechanism. We have completely revised Section 3.4.1 and added the 3D profile figures to incorporate this critical vertical dynamic analysis.

Lines 372-400:

3.4.1 3D regional transport and synoptic subsidence

To explore the triggering factors for the occurrence of NOI days under the four weather types, we investigated the 3D regional backward trajectories and CWT spatial distributions (Figs. 8, 9 and S8). While horizontal advection determines the regional source regions, the vertical profiles of these trajectories provide crucial Lagrangian evidence of downward transport.

Under A-type, air masses predominantly originated from the north (58.69%) (Fig. 8(a)). Crucially, the 3D altitude profiles (Fig. S8(a)-(b)) reveal that these dominant clusters originated from significantly high altitudes (~800 hPa) 48 hours prior, exhibiting continuous and massive subsidence as they approached Xinxiang. When these subsiding trajectories passed over the high O_3

potential source areas in northern Henan and western Shandong (CWT: 90-100 μg m^{-3}; Fig. 9(a)), regions well-documented for their heavy industrial facilities and intense precursor emissions (Lu et al., 2019; Li et al., 2019), they effectively entrained O_3-rich air from the residual layer downwards.

Under C-type, the airflow exhibited shorter trajectories and slower movement. Notably, the trajectory profile (Fig. S8(c)-(d)) captures an extremely dramatic vertical intrusion, where a specific cluster (21.43%) plunged directly from the lower free troposphere (~700 hPa, >2000 m) down to the surface. This intense vertical transport, coupled with high CWT values (~80 μg m^{-3}) over central/northern Henan (Fig. 9(b)), highlights the profound impact of deep vertical exchange driven by the cyclonic system.

Influenced by strong geostrophic winds under S-type, southwest airflow pathways dominated (Fig. 8(c)). The CWT analysis (Fig. 9(c)) identified a vast high-value source region (WCWT > 100 μg m^{-3}) encompassing the Central China urban agglomeration to the south, a vast region where intense anthropogenic NO_x and VOCs emissions continuously fuel massive daytime photochemical O_3 accumulation. The vertical profiles (Fig. S8(e)-(f)) confirm that a major portion of this southerly advection (~45.29%) subsided from the upper boundary layer (~880 hPa).

Finally, under WNE-type, the horizontal airflow was mainly concentrated on the northwest direction, accounting for 61.67% (Fig. 8(d)). The corresponding 3D altitude profiles (Fig. S8(g)-(h)) still capture a clear downward transport signal, revealing that this primary cluster originated from the upper residual layer (~800 hPa) 48 hours prior and subsided continuously. As these subsiding air masses passed over the potential source regions localized in central and northern Henan (CWT: 70-80 μg m^{-3}; Fig. 9(d)), they facilitated the downward entrainment and transport of O_3 to Xinxiang.

In summary, the 3D trajectory analysis demonstrates that the nocturnal O_3 spikes in Xinxiang are not merely driven by surface-level horizontal advection. Across all four weather types, the surface-arriving air masses systematically originated from the upper boundary layer or lower free troposphere, providing undeniable Lagrangian evidence of continuous downward O_3 transport from high-altitude reservoirs.

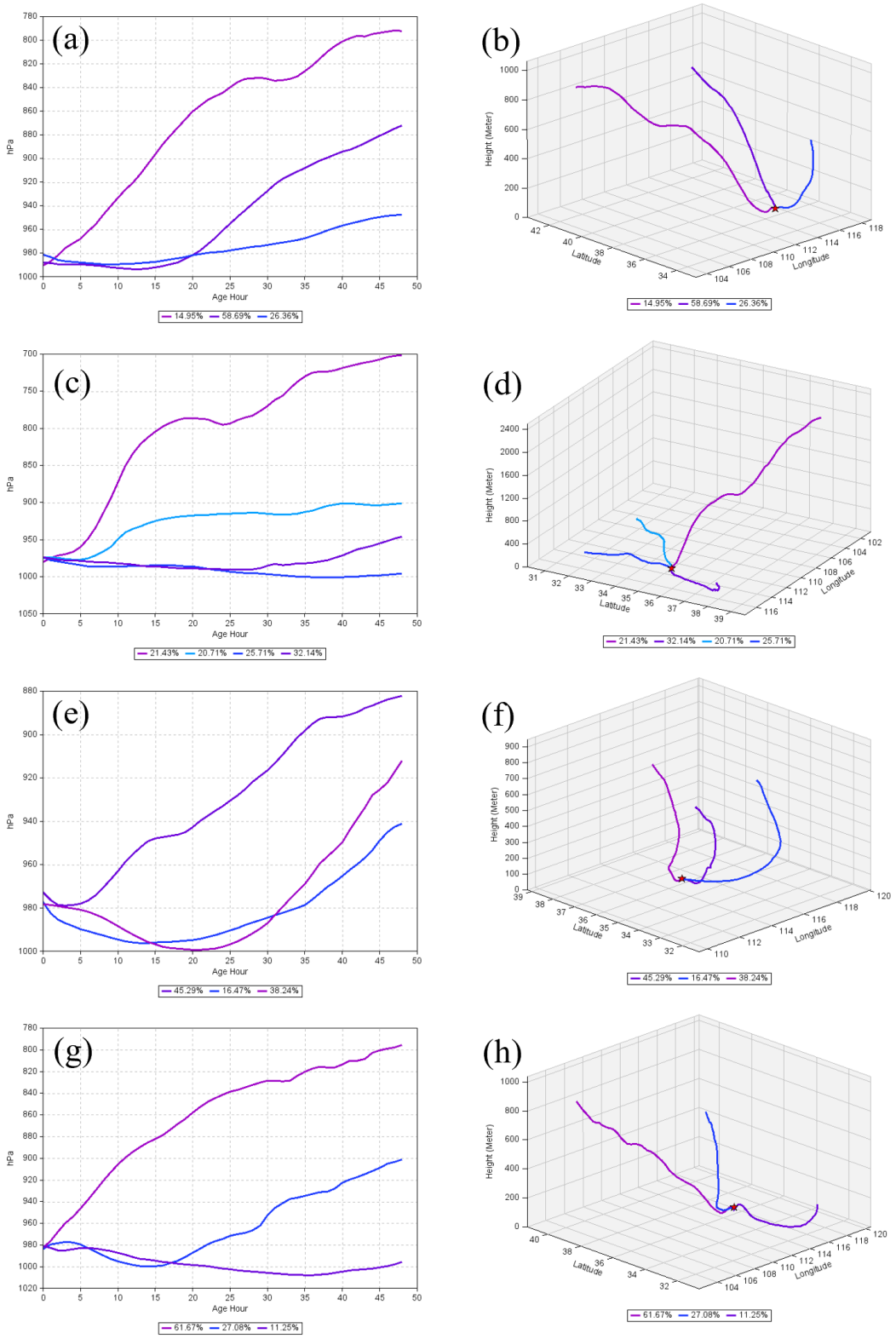


Figure S8: 3D clustered backward trajectories and their corresponding vertical pressure profiles for air masses arriving at Xinxiang under the four weather types. The left column (a), (c), (e), (g) displays the altitude-time cross-sections (represented by atmospheric pressure, hPa) of the trajectory clusters over the 48-hour backward tracking period. The right column (b), (d), (f), (h) illustrates the 3D spatial pathways of these clusters. The four

rows from top to bottom correspond to A-type (a, b), C-type (c, d), S-type (e, f), and WNE-type (g, h), respectively. The red star denotes the receptor site (Xinxiang). The percentages in the legends indicate the relative contribution of each trajectory cluster to the total trajectories under that specific weather type.

5. Causal Connections: While the manuscript provides a detailed description of meteorological features, it fails to sufficiently link these features to the underlying ozone phenomenology. The discussion often focuses on meteorological variables that may not be the primary drivers of ozone variability, leaving the physical connection between transport types and NOI poorly resolved.

Response 5: Thanks for reviewer's comments. The original manuscript, the discussion of meteorological features was overly descriptive and failed to explicitly establish the actual physical and dynamical pathways driving the nocturnal O_3 enhancements.

To address this critical flaw and establish the causal connections between weather types and the local O_3 phenomenology, we have completely restructured and rewritten Section 3.3. Instead of merely listing descriptive meteorological variables, the revised Section 3.3 now strictly constructs a causal chain for each weather type: macro-synoptic forcing, localized boundary-layer mechanical/thermodynamic perturbation and downward O_3 intrusion.

Specifically, we have explicitly resolved the physical causal connections through the following distinct pathways in the revised text:

(1) High-pressure subsidence (A-type): For calm conditions, we established a strict thermodynamic linkage. We explicitly linked the anticyclonic synoptic forcing to a highly stable, suppressed local environment with negative friction velocity anomalies (mean: $\Delta U^* = -0.01$ m s^{-1}). This severely suppresses general surface mechanical turbulence, serving as the essential thermodynamic and physical precondition that allows large-scale, high-pressure subsidence to dominate the column.

(2) Convective downdrafts and cold pools (C-type): Rather than simply mentioning general seasonal humidity, we causally linked the cyclonic low-pressure background and warm-wet moisture transport (mean: $\Delta RH = 4.08\%$) to amplified atmospheric thermodynamic instability.

(3) Intense mechanical shear and turbulent mixing (S-type & WNE-type): We shifted the focus from general wind speeds to specific mechanical turbulence metrics. As demonstrated in the revised

text, the intense synoptic pressure gradients directly cause massive localized spikes in friction velocity (mean: $\Delta U^* = 0.11$ m s^{-1} and 0.06 m s^{-1}) and massive boundary layer lifting (mean: $\Delta PBLH > 100$ m).

Instead of merely summarizing these changes, we want to transparently demonstrate how this causal logic has been explicitly woven into the narrative. Please find the fundamentally rewritten text of Section 3.3, which strictly follows this causal chain, provided below:

Lines 307-367:

3.3 Meteorological characteristics of primary weather types

As established in Section 3.1, the vast majority of NOI events in Xinxiang occur during the LN period. During this phase, the nocturnal boundary layer is characterized by a fully established surface inversion, creating a highly stable thermodynamic environment. To trigger downward O_3 transport under such extreme stability, localized residual turbulence is entirely insufficient. Instead, it requires massive, active mechanical forcing capable of physically breaking the inversion layer. Because such powerful mechanical triggers are fundamentally governed by macro-scale weather systems, identifying the specific synoptic circulations is the critical next step to unravel the forcing mechanisms behind these NOI events.

It should be noted that while seasonal variations significantly influence the daytime photochemical generation and absolute background concentrations of O_3, the nocturnal occurrence of NOI is predominantly driven by physical transport. As validated by the seasonal comparison (Fig. S6 and Text S3), while the absolute intensity of meteorological variables naturally fluctuates across seasons, the fundamental dynamical frameworks for a given weather type (e.g., the general orientation of horizontal pressure gradients and patterns of vertical motions) maintain functionally comparable mechanical triggers. Therefore, rather than focusing on seasonal background variations, our study focuses on elucidating these primary, synoptically-driven local meteorological drivers that trigger NOI.

The representative NOI days in Xinxiang were classified into four weather types (A-type, C-type, S-type, and WNE-type), with each exhibiting distinct meteorological features. Fig. 7 illustrates the spatial distributions of 850 hPa wind fields under four weather types. Under A-type, Xinxiang was located near a high-pressure center, with an outward-rotating wind field at 850 hPa (Figs. 5(a) and 7(a)), indicating the presence of an anticyclonic high-pressure system. Driven by this

synoptic forcing, Xinxiang experienced extremely calm conditions. As explicitly demonstrated by the nocturnal anomalies in Fig. 6 and Table S2, A-type was characterized by negative anomalies in wind speed (mean: ΔWS = -0.10 m s^{-1}) and friction velocity (mean: ΔU^* = -0.01 m s^{-1}), alongside a strongly constrained boundary layer (mean: $\Delta PBLH$ = 3.56 m, representing negligible expansion). This indicates that the overriding high-pressure system creates a highly stable environment. The explicit intrusion process of O_3 under this subsidence will be further verified in Section 3.4.

Under C-type, Xinxiang was dominated by low-pressure systems (Fig. 5(b)). At 850 hPa, a strong airflow originating near the coastal region of Guangxi Province moved continuously northeastward (Fig. 7(b)). This airflow not only moved at a high speed, but also likely carried substantial moisture, significantly enhancing atmospheric instability in its trajectory and surrounding regions (including Xinxiang), intensifying convective activity, and increasing the risk of heavy rainfall. Combined with the water vapor flux and divergence fields at 850 hPa, we find that the intense southwest warm-wet moisture transport belt under C-type is extremely prominent. Significant moisture convergence is observed along the entire path of this belt (including Xinxiang) (Fig. S7). Notably, the local meteorological anomalies perfectly capture this advection, with C-type uniquely coinciding with distinct positive anomalies in temperature (mean: ΔT = 2.60 °C) and the highest relative humidity anomaly among all weather types (mean: ΔRH = 4.08%). This localized warm and highly humid environment, dynamically coupled with a cyclonic low-pressure background, significantly amplifies atmospheric thermodynamic instability, highly favoring the development of regional convection and precipitation. Consequently, rather than uniform large-scale subsidence, NOI under C-type is primarily triggered by convective downdrafts and the subsequent development of cold pools.

S-type represents a dynamic environment driven by distinct horizontal advection. Under S-type, Xinxiang was situated in a tight pressure gradient, typically between a western low and an eastern high (Figs. 5(c) and 7(c)). Driven by this synoptic setup, continuous southerly geostrophic winds prevailed over the region. As detailed in Table S2, S-type produced significant positive anomalies in local wind speed (mean: ΔWS = 0.54 m s^{-1}) and friction velocity (mean: ΔU^* = 0.06 m s^{-1}). These specific values rigorously demonstrate that beyond facilitating regional horizontal transport (which will be explicitly traced in Section 3.4.1), the southerly advection directly generates substantial localized mechanical turbulence at the surface, physically lifting the nocturnal boundary layer

(mean: ΔPBLH = 102.41 m). This localized mechanical shear serves as the direct trigger for breaking nocturnal stability, subsequently entraining O_3-rich air from the elevated residual layer down to the surface and triggering NOI events.

Although Xinxiang often featured a massive continental high-pressure system (e.g., the Siberian High) to the northwest under WNE-type (Fig. 5(d)), their local dynamics are fundamentally different from the pure subsidence of A-type. At 850 hPa, the region was obviously influenced by a northwestern airflow (Fig. 7(d)), consistent with the geostrophic wind characteristics of WNE-type. Unlike A-type, where the study area sits calmly at the high-pressure center, under WNE-type, Xinxiang was located at the densely packed periphery of the advancing high. Consequently, the macroscopic forcing shifts to intense horizontal pressure gradients (Figs. 5(d) and 7(d)). This kinematic distinction is perfectly captured by the localized surface anomalies (Table S2). WNE-type exhibited the most extreme positive anomalies among all categories, with local wind speed (mean: ΔWS = 1.74 m s^{-1}) and friction velocity (mean: ΔU^* = 0.11 m s^{-1}) far exceeding other types. Driven by this intense horizontal advection and wind shear, the nocturnal boundary layer experienced massive mechanical lifting (mean: ΔPBLH = 156.22 m). Furthermore, this intense mechanical mixing effectively breaks the nocturnal surface inversion, bringing slightly warmer air from aloft downward (detailed mechanism analysis is presented in Section 3.4.2). This vigorous downward mixing of the elevated residual layer shares conceptual similarities with the nocturnal fumigation-like processes documented in other literature (Wu et al., 2023; He et al., 2022), which also explains the observed positive temperature anomaly (mean: ΔT = 0.77 °C). Therefore, despite the high-pressure background, it is this extraordinarily strong localized shear and turbulent mixing, that serves as the primary mechanical driver forcing O_3 downward to the surface during WNE-type. Combined with rapid dispersion of local NO emissions under high winds that greatly mitigates nighttime titration, vigorous vertical entrainment counteracts both horizontal diffusion and titration loss of O_3, and ultimately causes a net O_3 surge.

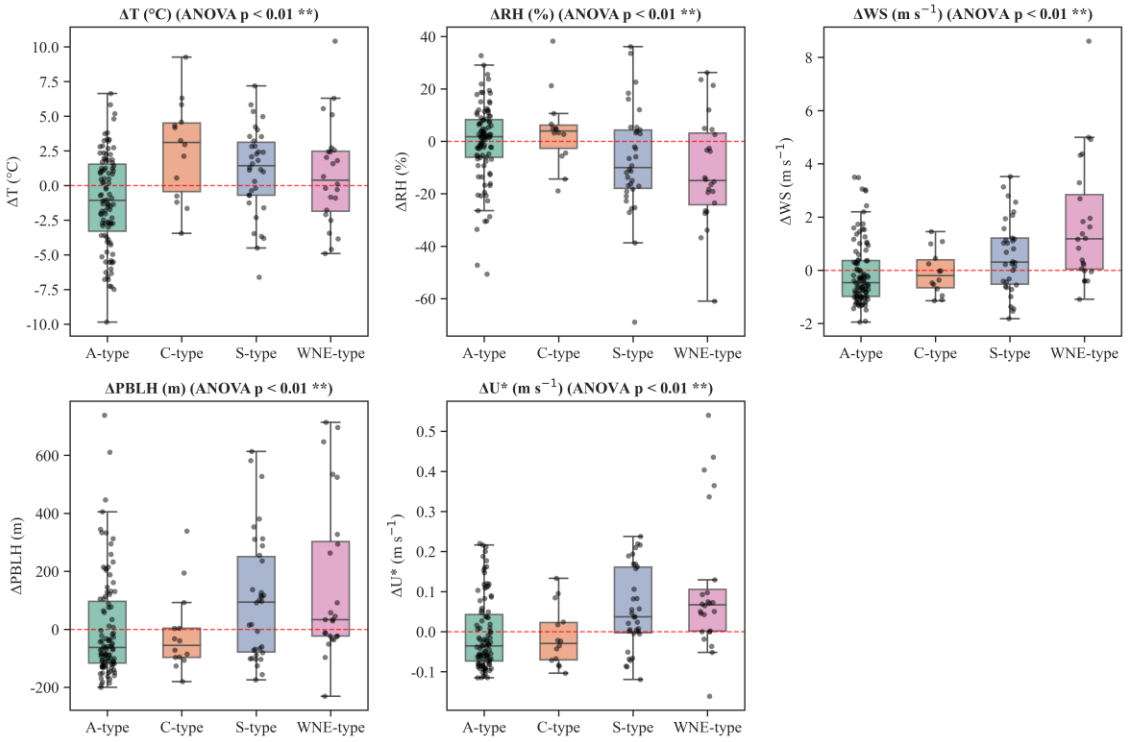


Figure 6: One-Way ANOVA results for key meteorological variables (T, RH, WS, PBLH and U^*) of different synoptic categories. In each boxplot, the central black solid line indicates the median. The horizontal red dashed line denotes the zero-anomaly reference.

Table S2. Statistical summary of nocturnal meteorological anomalies and ANOVA results under the four weather types.

Variable	A-type	C-type	S-type	WNE-type	p-value
ΔT (°C)	-1.07 ± 3.41	2.60 ± 3.54	1.06 ± 3.18	0.77 ± 3.70	$< 0.01^{**}$
ΔRH (%)	-0.31 ± 14.82	4.08 ± 14.00	-7.12 ± 20.46	-11.15 ± 20.72	$< 0.01^{**}$
ΔWS (m s^{-1})	-0.10 ± 1.21	-0.08 ± 0.83	0.54 ± 1.39	1.74 ± 2.32	$< 0.01^{**}$
ΔPBLH (m)	3.56 ± 178.15	-14.44 ± 139.19	102.41 ± 216.82	156.22 ± 274.82	$< 0.01^{**}$
ΔU^* (m s^{-1})	-0.01 ± 0.09	-0.01 ± 0.07	0.06 ± 0.10	0.11 ± 0.17	$< 0.01^{**}$

Note: Data are presented as Mean ± Standard Deviation. The anomalies (Δ) were calculated relative to their respective monthly nocturnal means. The p-values are derived from One-Way ANOVA tests indicating statistical significance under the four weather types.

6. The occurrence of NOI cannot be related solely with long-range transport ignoring local/regional features.

Response 6: Thanks for reviewer's comments. We have restructured the manuscript (specifically

Section 3.4.2) to explicitly couple overarching synoptic transport with critical local/regional features.

As detailed in the revised manuscript, we have now incorporated several key local features to explain the physical triggering of NOI:

(1) Subsidence-driven compression (A-type): This weather type is strictly dominated by systematic high-pressure subsidence. Wind shear breaks down the nocturnal inversion layer, increasing near-surface atmospheric instability and intensifying turbulent mixing, which transports O_3 from the residual layer down to the surface.

(2) Thermodynamically-driven convective mixing (C-type): Distinct from uniform subsidence, this mechanism is driven by localized mesoscale thermodynamics. Triggered by a cyclonic low-pressure background and intense moisture advection, the downward transport is dominated by the cold-pool downdrafts and shallow convection.

(3) Shear-driven mechanical entrainment (S-type and WNE-type): Both of these patterns are primarily controlled by synoptically-driven intense wind shear, utilizing massive horizontal advection to physically rupture the nocturnal inversion layer.

In our current narrative, regional transport (Section 3.4.1) is explicitly framed merely as the delivery mechanism that supplies the high-altitude O_3 reservoir, while the local and regional features (Section 3.4.2) are identified as the essential mechanical triggers that bring it down to the surface.

Lines 406-451:

3.4.2 Vertical mixing and mechanical triggers

As established in Section 3.4.1, 3D trajectories confirm the synoptic delivery of air masses from high altitudes. However, to translate these high-altitude arrivals into surface NOI events, specific vertical transport mechanisms are required. To validate this process, we analyzed the vertical profiles of pressure velocity (Fig. 10), thermodynamic stability (Fig. S9), O_3 concentrations (Fig. S10), and surface turbulence metrics (Fig. 11).

The vertical O_3 profiles (Fig. S10) first confirm the fundamental prerequisite for NOI across all weather types: following sunset, a distinct nocturnal residual layer (RL) forms, clearly indicated by the high O_3 concentrations. Shielded from surface NO titration and dry deposition, this RL successfully retains high daytime O_3, serving as the localized O_3 reservoir waiting to be tapped by

downward forcing.

For A-type, the intrusion is primarily initiated by the systematic macroscopic subsidence of the continental high-pressure system. As explicitly shown in Fig. 10(a), a robust macro-scale downdraft dominates the vertical column over the Xinxiang region. This subsidence induces profound adiabatic compression, forming a significant low-level temperature inversion (1000-950 hPa) accompanied by low mid-level RH (Fig. S9). The inversion layer acts as a dynamic barrier, leading to marked vertical gradients in horizontal wind and sinking velocity and generating localized vertical wind shear. While the overall nocturnal surface environment remains highly stable and suppressed (consistent with the negative mean ΔU^* anomaly in Table S2), this localized shear interaction triggers intermittent, transient bursts of mechanical turbulence. These brief turbulent eddies, evidenced by the distinct nocturnal fluctuations in U^* (Fig. 11), provide enough mechanical mixing to efficiently entrain the O_3-rich air from the residual layer down to the surface.

Under C-type, vertical mixing is dominated by localized mesoscale thermodynamics rather than uniform synoptic subsidence. As seen in Fig. 10(b), the vertical velocity field exhibits a complex coexistence of localized downdrafts and updrafts. The thermodynamic profiles (Fig. S9) corroborate this with a temperature inversion and mid-level dry air entrainment. This aligns perfectly with the cold pool mechanism: following convective rainfall, surface evaporative cooling generates a dense, subsiding pool of cold air. Simultaneously, the moderate CAPE values (86-314 J kg^{-1}) indicate residual thermodynamic instability driving localized shallow convection. The intense collision between these subsiding cold pools and localized convective motions creates severe turbulent mixing. This translates into the sharp nocturnal fluctuations in U^* (Fig. 11), thereby increasing instability and dragging O_3-rich air from the RL into the surface.

The local triggering mechanism under S-type relies fundamentally on intense mechanical shear overriding macro-scale lifting. S-type features strong southerly geostrophic winds. As this intense airflow approaches Xinxiang, it is forced upward by the Taihang Mountains, generating pronounced macro-scale orographic updrafts (Fig. 10(c)). However, to achieve the downward transport of O_3 against this macroscopic background lifting, a highly aggressive, localized boundary-layer mixing mechanism is essential. Specifically, the moderate CAPE values (257-295 J kg^{-1}) indicate persistent thermodynamic instability (Fig. S9), which fuels localized shallow convective motions within the nocturnal boundary layer. Simultaneously, anomalously strong near-surface horizontal winds (mean:

ΔWS = 0.54 m s^{-1}; Table S2) forcefully interact with surface friction, inducing severe mechanical wind shear. The powerful synergy of this thermal instability and mechanical shear explicitly manifests as massive, sharp nocturnal spikes in U^* and PBLH (Table S2 (mean: ΔPBLH = 102.41 m, ΔU^* = 0.06 m s^{-1}) and Fig. 11). Ultimately, this exceptionally enhanced turbulent mixing mechanically erodes the stable nocturnal inversion, overpowering the macroscopic updrafts to aggressively drag aloft O_3 from the residual layer down to the surface.

Finally, under WNE-type, downward transport is facilitated by an advection-driven mechanical shear mechanism. As explicitly shown in Fig. 10(d), the lower troposphere (below 850 hPa) is dominated by intense macro-scale subsidence. This induces a strong temperature inversion and extreme thermodynamic stability, corroborated by low CAPE values (22-23 J kg^{-1}) (Fig. S9), meaning thermal convective motions are completely suppressed. However, WNE-type is simultaneously driven by intense horizontal advection. As this robust horizontal airflow passes over Xinxiang, intense near-surface vertical wind shear is produced. This macroscopic advective forcing translates directly into massive nocturnal spikes in boundary-layer turbulence, explicitly captured by U^* and PBLH (Table S2 (mean: ΔPBLH = 156.22 m, ΔU^* = 0.11 m s^{-1}) and Fig. 11). This enhanced nocturnal turbulence drives the downward transport of O_3 from the residual layer to the surface, thereby triggering the NOI events.

Specific comments:

1. Line 48: Please expand on the specific negative impacts of NOI to underscore the environmental importance of the study.

Response 1: Thanks for reviewer's comments. We have expanded the relevant discussion in the Introduction. Rather than solely focusing on the direct health effects, we have now detailed three major environmental and atmospheric consequences of NOI:

(1) Direct toxicity: Rapid surges in nighttime O_3 (occasionally surpassing 160 μg m^{-3}) directly pose nocturnal threats to human health and exacerbate plant stomatal uptake.

(2) Exacerbation of daytime photochemical smog: We emphasized that horizontal or vertical transport of O_3-rich air elevates the surface O_3 baseline for the following morning, accelerating daytime accumulation and worsening subsequent photochemical smog.

(3) Alteration of atmospheric oxidative capacity (AOC): We linked NOI to the broader issue of regional fine particulate matter ($PM_{2.5}$) pollution, explaining how enhanced nocturnal O_3 facilitates dark reactions (generating NO_3 and N_2O_5), which are critical precursors for secondary organic aerosols (SOA) and particulate nitrates.

Lines 45-55:

Although a quantitative threshold of a 10 μg m^{-3} hourly increase may appear modest during a clean night, the scientific and environmental significance of NOI episodes extends far beyond simple numerical detection. First, NOI events can occasionally result in a rapid surge in nighttime O_3 levels surpassing 160 μg m^{-3} (Wang et al., 2023b; Zhu et al., 2024), directly posing nocturnal threats to human health and plant stomatal uptake (Chowdhury et al., 2022; Hoshika et al., 2019). More critically, even when absolute concentrations remain moderate, the horizontal or vertical transport of O_3-rich air that typically triggers NOI significantly elevates the surface O_3 baseline for the following morning. This higher initial baseline accelerates daytime accumulation, effectively exacerbating subsequent daytime photochemical smog (Wang et al., 2025). Furthermore, unexpected nighttime O_3 increments fundamentally alter the nocturnal atmospheric oxidative capacity (AOC). The enhanced O_3 facilitates dark reactions with nitrogen dioxide (NO_2) to generate nitrate radicals (NO_3) and dinitrogen pentoxide (N_2O_5), critical precursors for particulate nitrate and secondary organic aerosols (SOA), thereby linking NOI directly to regional fine particulate matter ($PM_{2.5}$) pollution (Wang et al., 2023a).

2. Line 64: Provide more comprehensive metadata for the study area, including population density in Xinxiang, primary precursor sources, and general climatological characteristics.

Response 2: Thanks for reviewer's comments. In the revised manuscript (Introduction), we have expanded the description of the study area to include the three specific aspects reviewer suggested:

(1) Population metadata: We added the demographic context, noting that Xinxiang is a densely populated urban center with a population exceeding 6 million and a density of over 700 persons km^{-2}.

(2) Climatological characteristics: We specified that the region experiences a typical temperate continental monsoon climate, characterized by hot, humid summers and cold, dry winters.

(3) Primary precursor sources: We clarified that the primary O_3 precursors (NO_x and VOCs)

predominantly originate from local heavy industrial facilities (e.g., chemical and manufacturing plants), intense vehicular exhaust from its transportation networks, and solvent usage.

By incorporating these detailed regional characteristics, the rationale for selecting Xinxiang as a critical representative case study in the North China Plain has been greatly strengthened.

Lines 73-80:

Located in the southern NCP, Xinxiang is bordered by the Taihang Mountains to the north and the Yellow River to the south (Fig. S1). As a densely populated urban center (with a population exceeding 6 million and a high population density of over 700 persons km^{-2}), Xinxiang features a typical temperate continental monsoon climate, characterized by hot, humid summers and cold, dry winters. Furthermore, serving as a major industrial and transportation hub in Henan Province, the city experiences intense anthropogenic emissions. The primary precursors for O_3 (i.e., NO_x and VOCs) predominantly originate from heavy industrial facilities (e.g., chemical and manufacturing plants), intense vehicular exhaust along major transportation arteries, and solvent usage. This unique topography, combined with these high baseline emissions and specific climatological conditions, makes Xinxiang a critical case study for understanding NOI.

3. Section 2.1: It is essential to specify the spatial and temporal resolutions of the MERRA-2 and ERA5 datasets used.

Response 3: Thanks for reviewer's comments. In the revised manuscript (Section 2.1), we have now added the spatial and temporal resolutions for both datasets:

Lines 99-103:

Sea level pressure (SLP) data and 17-layer vertical profiles (500-1000 hPa) of vorticity, wind speed (WS), wind direction, temperature (T), relative humidity (RH) and O_3 concentration were acquired from the Modern-Era Retrospective Analysis for Research and Applications dataset (MERRA-2, Version 2, with a spatial resolution of 0.5° × 0.625° and temporal resolutions of 1 hour for surface data and 3 hours for 3D vertical profiles) (https://disc.gsfc.nasa.gov/).

Lines 106-110:

Additionally, specific humidity (850hpa), planetary boundary layer height (PBLH), friction velocity (U^*), and convective available potential energy (CAPE) were derived from the ERA5

reanalysis dataset (https://www.ecmwf.int/en/forecasts/dataset/ecmwf-reanalysis-v5) (with a spatial resolution of 0.25° × 0.25° and an hourly temporal resolution) provided by the European Centre for Medium-Range Weather Forecasts (ECMWF), which offers superior boundary layer parameters (Hersbach et al., 2020; Bell et al., 2021).

4. Section 2.3: The use of Sea Level Pressure (SLP) for the Lamb-Jenkinson classification may overlook transport occurring at higher altitudes. I suggest incorporating data from higher geopotential heights to ensure the synoptic classification is representative of the layers where ozone transport is most active.

Response 4: Thanks for reviewer's comments. We have considered substituting the input data. However, we encountered a strict methodological limitation inherent to the Lamb-Jenkinson (L-J) objective weather typing method itself. We ultimately had to retain SLP as the primary input based on the following practical and physical considerations, but we took an alternative verification approach:

(1) The strict algorithmic constraint of the L-J method: The L-J classification algorithm is mathematically strictly defined and calibrated exclusively for Sea Level Pressure (SLP) fields. Its core mathematical framework and the specific threshold criteria used to assign the 27 weather types are rigidly normalized for surface-level pressure gradients. Attempting to substitute SLP with upper-level geopotential heights fundamentally breaks the method's original algorithmic constraints, making it impossible to derive valid classification indices.

(2) Cross-validating SLP types with high-altitude transport: To strictly adhere to the established L-J mathematical methodology while fully addressing reviewer's valid concern regarding high-altitude transport, we took an alternative verification approach. Because macro-scale synoptic systems are typically deep, equivalent-barotropic systems, we extracted the 850 hPa wind fields and overlaid them directly onto our SLP-derived weather types (Fig. S5).

As explicitly demonstrated in Fig. S5, the spatial patterns of the 850 hPa wind flow exhibit a near-perfect coupling with the SLP-defined synoptic types. This verification ensures that while our algorithm relies on SLP to satisfy its mathematical requirements, the resulting weather types successfully and comprehensively represent the very high-altitude transport circulations.

Lines 257-263:

Fig. S4 displays the mean SLP of representative NOI days under different weather types from 2021 to 2023. It can be seen that the position of high- and low-pressure centers exhibit certain discrepancies among different weather types. Furthermore, to explicitly validate that this SLP-based classification accurately captures airflow characteristics in lower troposphere, Fig. S5 illustrates the spatial distributions of mean SLP overlaid with 850 hPa wind fields for the 20 identified weather types. The spatial patterns demonstrate a high degree of physical consistency, wherein the surface pressure gradients align with the 850 hPa wind field. This confirms that the SLP-based Lamb-Jenkinson method is highly robust and effectively represents synoptic circulation background of upper boundary-layer.

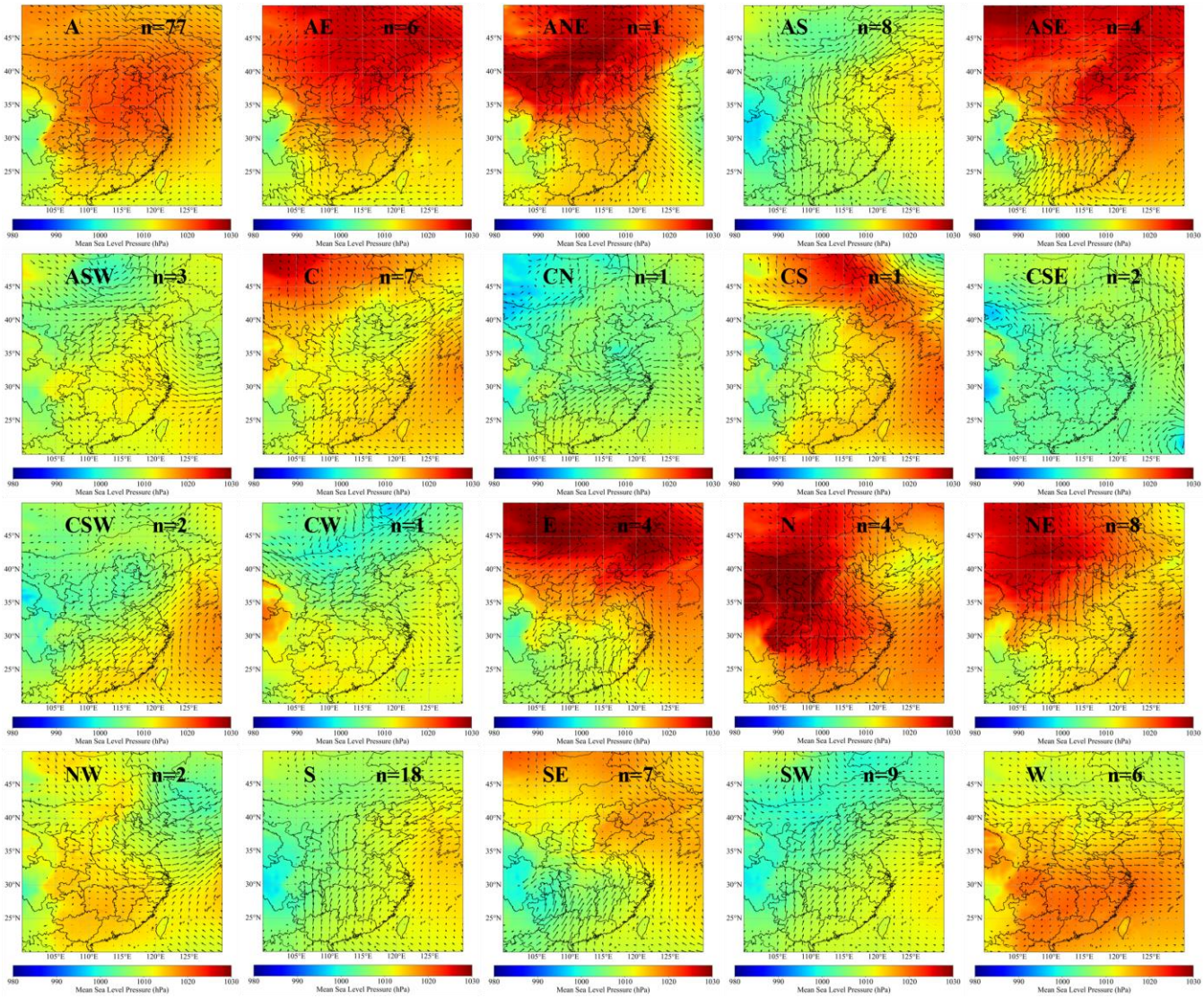


Figure S5: Spatial distribution of composite mean SLP and 850 hPa wind fields under different weather types (Preliminarily identified based on the Lamb-Jenkinson synoptic circulation classification method; n denotes the number of days).

5. Line 119: Please cite the HYSPLIT model formally (e.g., Stein et al., 2015).

Response 5: Thanks for reviewer's comments. We have now added the formal citation for the HYSPLIT model (Stein et al., 2015) to both the main text and the reference list.

Lines 164-165:

The hybrid single particle lagrangian integrated trajectory (HYSPLIT) is a common model for investigating meteorological transmission channels (Chen et al., 2024; Cheng et al., 2024; Shi et al., 2024; Stein et al., 2015).

6. Lines 131–136: Figure 1 indicates a secondary peak in June that is currently unaddressed. This feature should be interpreted in the context of seasonal ozone precursors or meteorological shifts.

Response 6: Thanks for reviewer's comments. The secondary peak in June is a crucial feature that requires explicit interpretation through the lens of seasonal precursor dynamics and meteorological shifts.

We have expanded our discussion to explicitly address this phenomenon. We now explain that the June peak is fundamentally driven by the coupling of these two factors:

(1) Meteorological shifts: June marks the onset of summer in the NCP, characterized by soaring temperatures and intensified solar radiation.

(2) Seasonal precursors: These warmer meteorological conditions directly trigger enhanced emissions of seasonal O_3 precursors (particularly biogenic VOCs).

The combination of abundant precursors and favorable photochemistry drives massive daytime O_3 accumulation. This generates a highly concentrated O_3 residual layer by dusk, which provides an abundant aloft reservoir that facilitates the occurrence of NOI events during this month.

Lines 183-193:

Additionally, all stations showed similar monthly variation trends: NOI days progressively increased from January to March, peaking in March (42-47 days), and then maintained high-level fluctuations from April to September. Notably, a distinct secondary peak is observed in June (Fig. 1). This early summer peak can be primarily attributed to the coupled effects of seasonal meteorological shifts and O_3 precursor dynamics. Meteorologically, June marks the transition to

summer in the NCP, characterized by sharp increases in temperature and intensified solar radiation. Concurrently, these warmer conditions significantly stimulate the enhanced emissions of natural ozone precursors (e.g., biogenic VOCs). The combination of abundant precursors and highly favorable meteorological conditions drives intense daytime photochemical O_3 production. This vigorous daytime accumulation generates a highly concentrated O_3 residual layer by dusk, which ultimately acts as an abundant aloft source for NOI events. Subsequently, the frequency reaches another peak in September (32-44 days) before declining sharply from October to December, reaching annual minima (15-26 days). This indicated that warm seasons favor NOI occurrence.

7. Section 3.4.1: When identifying geographical source areas via back-trajectories, the authors should discuss the known precursor emission profiles of those regions to provide a more robust chemical context.

Response 7: Thanks for reviewer's comments. In the revised Section 3.4.1, we have added the necessary chemical context to the key source regions identified by the back-trajectories:

(1) For A-type: We highlighted that northern Henan and western Shandong are regions well-documented for their heavy industrial facilities and intense precursor emissions.

(2) For S-type: We specified that the Central China urban agglomeration is characterized by intense anthropogenic NO_x and VOCs emissions, which act as the fundamental fuel for the massive O_3 accumulation observed in our CWT results.

By briefly contextualizing these emission profiles, the manuscript now provides a more robust bridge between the regional photochemical generation (daytime) and the subsequent advective/vertical transport (nighttime).

Lines 376-381:

Under A-type, air masses predominantly originated from the north (58.69%) (Fig. 8(a)). Crucially, the 3D altitude profiles (Fig. S8(a)-(b)) reveal that these dominant clusters originated from significantly high altitudes (~800 hPa) 48 hours prior, exhibiting continuous and massive subsidence as they approached Xinxiang. When these subsiding trajectories passed over the high O_3 potential source areas in northern Henan and western Shandong (CWT: 90-100 μg m^{-3}; Fig. 9(a)), regions well-documented for their heavy industrial facilities and intense precursor emissions (Lu et al., 2019; Li et al., 2019), they effectively entrained O_3-rich air from the residual layer downwards.

Lines 387-391:

Influenced by strong geostrophic winds under S-type, southwest airflow pathways dominated (Fig. 8(c)). The CWT analysis (Fig. 9(c)) identified a vast high-value source region (WCWT > 100 μg m^{-3}) encompassing the Central China urban agglomeration to the south, a vast region where intense anthropogenic NO_x and VOCs emissions continuously fuel massive daytime photochemical O_3 accumulation. The vertical profiles (Fig. S8(e)-(f)) confirm that a major portion of this southerly advection (~45.29%) subsided from the upper boundary layer (~880 hPa).

Reviewer #3

Methodological Issues:

1. NOI significance is not addressed. The definition of a NOI event does not account for baseline ozone levels. An increase of 10 ug/m^3 over a baseline of 70 ug/m^3 is not equivalent to the same increase over 120 ug/m^3. Similarly, the temporal trajectory matters: a 10 ug/m^3 rise followed by an immediate decline is fundamentally different from a sustained or accelerating increase. These dimensions must be incorporated into the event detection framework.

Response 1: Thanks for reviewer's comments. We rigorously re-evaluated our event detection framework. We ultimately retained the standard >10 μg m^{-3} per hour absolute increment threshold, but we realized that our original manuscript failed to explicitly articulate why this choice was deliberately made to serve the specific dynamic focus of this study. We have now addressed this extensively in the revised text based on the following scientific rationales:

(1) Using absolute increment as a pure proxy for physical transport: The core objective of this study is to unravel the synoptic-scale meteorological drivers (e.g., strong wind shear, regional subsidence) that physically break the nocturnal inversion. From a fluid dynamics perspective, a sudden hourly surge of >10 μg m^{-3} indicates that a rapid, massive downward or horizontal physical transport has abruptly overpowered the local nocturnal depletion (titration and deposition). This absolute increment acts purely as a mathematical proxy for the mechanical transport, independent of the background chemical baseline. This absolute increment threshold is currently the widely accepted standard in meteorological NOI studies (Zhu et al., 2020; He et al., 2022; Wang et al., 2025; Wang et al., 2023b).

(2) Clarifying the significance of NOI in the revised text: To ensure readers do not conflate our physical detection metric with a health exposure assessment, we have expanded our narrative:

In the revised Introduction: We now discuss the broad significance of NOI regardless of the initial baseline. We clarified that these nocturnal intrusions critically elevate the surface baseline for the following morning (exacerbating next-day photochemical smog) and fundamentally alter the nocturnal atmospheric oxidative capacity (AOC) by fueling NO_3 and N_2O_5 chemistry.

In the revised Methodology (Section 2.2): We have added a dedicated paragraph explicitly defining the scope of this study. We acknowledge that while baseline is crucial for exposure

assessments, the absolute hourly increment is maintained as a robust indicator for detecting the timing and occurrence of pure meteorological physical intrusions.

Lines 43-55:

NOI events, characterized by unexpected rises in nighttime O_3 concentrations (at least 10 μg m^{-3} per hour (Zhu et al., 2020)), challenge the conventional understanding of O_3 (Wang et al., 2023b; Xue et al., 2023; Chen et al., 2024b). Previously, nocturnal O_3 was often overlooked owing to its low concentrations. Although a quantitative threshold of a 10 μg m^{-3} hourly increase may appear modest during a clean night, the scientific and environmental significance of NOI episodes extends far beyond simple numerical detection. First, NOI events can occasionally result in a rapid surge in nighttime O_3 levels surpassing 160 μg m^{-3} (Wang et al., 2023b; Zhu et al., 2024), directly posing nocturnal threats to human health and plant stomatal uptake (Chowdhury et al., 2022; Hoshika et al., 2019). More critically, even when absolute concentrations remain moderate, the horizontal or vertical transport of O_3-rich air that typically triggers NOI significantly elevates the surface O_3 baseline for the following morning. This higher initial baseline accelerates daytime accumulation, effectively exacerbating subsequent daytime photochemical smog (Wang et al., 2025). Furthermore, unexpected nighttime O_3 increments fundamentally alter the nocturnal atmospheric oxidative capacity (AOC). The enhanced O_3 facilitates dark reactions with nitrogen dioxide (NO_2) to generate nitrate radicals (NO_3) and dinitrogen pentoxide (N_2O_5), critical precursors for particulate nitrate and secondary organic aerosols (SOA), thereby linking NOI directly to regional fine particulate matter ($PM_{2.5}$) pollution (Wang et al., 2023a).

Lines 116-125:

NOI event is defined as an hourly O_3 concentration increment exceeding 10 μg m^{-3} during nighttime (20:00-06:00 local time, LT; UTC+8, Beijing Time) (He et al., 2021; Zhu et al., 2020). This absolute increment threshold is widely adopted in current literature (Zhu et al., 2024; Zhu et al., 2020; He et al., 2022; Wang et al., 2025) because it acts as an indicator for detecting the abrupt physical intrusion of O_3-rich air masses into local surface. While the absolute baseline concentrations and temporal trajectories of O_3 are crucial for evaluating human health exposure and long-term air quality attainment, the primary objective of this study is to isolate the underlying synoptic and meteorological transport mechanisms. Regardless of the initial surface baseline, a

sudden hourly surge of >10 μg m^{-3} effectively and consistently flags that sudden dynamic transport processes (whether via robust horizontal advection, massive vertical subsidence, or other regional intrusions) have completely overpowered the steady local nocturnal depletion (e.g., NO titration and dry deposition). Therefore, this increment-based metric provides the most robust and objective foundation for our dynamical and meteorological analysis.

2. The separation of night and morning periods is not adequately justified. While the intent is presumably to identify isolated days, this artificial split breaks the continuity of nocturnal dynamics. An increase beginning at night may well persist or evolve into the morning hours, and this continuity is lost under the current approach.

Response 2: Thanks for reviewer's comments. To address this exact issue and preserve the unbroken evolution of nocturnal transport, we have revised our temporal definition in the revised manuscript (Section 2.2).

Instead of an artificial calendar-day split, our event detection framework now treats the physical night as a single, continuous process. As stated in the revised text: "Since nighttime generally lasts from 20:00 to 06:00 LT the next day, it constitutes a continuous process. Therefore, a day is classified as an NOI day if such events occur from 20:00 to 06:00 LT the next day. By strictly confining the concept of NOI days to this continuous nocturnal window, we ensure that our dynamic analysis remains completely isolated from daytime photochemical interference." (Note: The morning cut-off is physically mandated by local sunrise to strictly prevent daytime contamination, and not to artificially break nocturnal continuity).

Under this revised continuous framework, an event that begins in the early night and persists into the morning hours is successfully captured as a single, uninterrupted event. Furthermore, to statistically describe when these events occur within this continuous night without using arbitrary mathematical intervals, we introduced three types that perfectly align with the physical evolution phases of the nocturnal boundary layer: (1) Early-night NOI (EN): The event occurs only between 20:00 and 23:00 LT, corresponding to the transitional boundary layer phase; (2) Late-night NOI (LN): The event occurs only between 00:00 and 06:00 LT, corresponding to the highly stable surface inversion phase; (3) Whole-night NOI (WN): The event occurs across both periods, persisting continuously through the night. These three sub-categories carry no other complex

implications, and they serve strictly as statistical labels.

Lines 126-137:

Considering the seasonal variation in local sunrise time, we excluded NOI events occurring after 05:00 LT from April to September, when the sunrise occurs relatively early. Since nighttime generally lasts from 20:00 to 06:00 LT the next day, it constitutes a continuous process. Therefore, a day is classified as an NOI day if such events occur from 20:00 to 06:00 LT the next day (excluding April to September, for which the window is 20:00 to 05:00 LT). By strictly confining the concept of NOI days to this continuous nocturnal window, we ensure that our dynamic analysis remains completely isolated from daytime photochemical interference. To further investigate the temporal occurrence characteristics within this continuous night, we subsequently categorized these NOI days into three descriptive types. Rather than using arbitrary mathematical intervals, the specific timeframes for these types were chosen to perfectly align with the distinct physical evolution phases of the nocturnal boundary layer: (1) Early-night NOI (EN): The event occurs only between 20:00 and 23:00 LT, corresponding to the transitional boundary layer phase; (2) Late-night NOI (LN): The event occurs only between 00:00 and 06:00 LT, corresponding to the highly stable surface inversion phase; (3) Whole-night NOI (WN): The event occurs across both periods, persisting continuously through the night.

3. The HYSPLIT methodology is described too briefly to be reproducible. As written, it would not allow an independent researcher to replicate the analysis. Furthermore, the Concentration-Weighted Trajectory (CWT) approach receives no methodological explanation whatsoever.

Response 3: Thanks for reviewer's comments. To ensure complete transparency and reproducibility, we have expanded Section 2.4 in the revised manuscript:

(1) Reproducibility of the HYSPLIT model: We have added the missing specific parameters required for independent replication. The revised text now explicitly details the spatial resolution of the GDAS data (1° × 1°), the temporal resolution of the trajectory calculations (at 1-hour intervals during the events), and clarifies the model execution environment.

(2) Methodological explanation of CWT: While the complete mathematical equations and weighting functions (W_{ij}) for the CWT approach were provided in Text S1 in the original

submission, we realize that a clear conceptual summary was missing from the main text. We have now incorporated a dedicated paragraph in Section 2.4 explaining the methodological mechanism of CWT. Specifically, how it calculates weighted average concentrations across grid cells to identify upwind source contributions, and how the empirical weighting coefficient mitigates uncertainties. We have also made the reference to the mathematical formulas in Text S1 much more prominent.

Lines 164-178:

The hybrid single particle lagrangian integrated trajectory (HYSPLIT) is a common model for investigating meteorological transmission channels (Chen et al., 2024; Cheng et al., 2024; Shi et al., 2024; Stein et al., 2015). It can efficiently and accurately determine the transport trajectories of different pollutants, classify and aggregate the backward trajectories during the study period through the Euler clustering method, and output air mass trajectories with different proportions. In this study, the HYSPLIT model (run via the TrajStat plugin / MeteoInfo) was used to identify backward trajectories for Xinxiang during the period from 2021 to 2023. The model inputs hourly meteorological data from the Global Data Assimilation System with a spatial resolution of 1° × 1° (ftp://arlftp.arlhq.noaa.gov/pub/archives/gdas1). Taking the starting point (central location of Xinxiang: 35.30°N, 113.88°E) as a reference, 48-hour backward trajectories terminating at 100 m above ground level were calculated at 1-hour intervals for all identified representative NOI days. Using these air mass trajectories, we mapped O_3 concentrations to specific geographic grids to apply Concentration-Weighted Trajectory (CWT) analysis. Briefly, the CWT approach calculates the weighted average concentration of air mass trajectories passing through each 1° × 1° grid cell, thereby quantitatively identifying the relative contributions of potential upwind source regions to local O_3 spikes (Shi et al., 2024; Wang et al., 2024). To mitigate statistical uncertainties from grid cells with sparse trajectory endpoints, an empirical weighting function W_{ij} was incorporated. The complete mathematical formulations and calculation parameters for the CWT methodology are detailed in Text S1.

4. The weather type classification lacks transparency. The identification and classification methodology appears highly subjective in its current description.

Response 4: Thanks for reviewer's comments. In the original manuscript, the aggregation of the detailed Lamb-Jenkinson (L-J) weather types into the four primary archetypes (A, C, S, and WNE)

was described too briefly, which may have given the impression of a subjective clustering approach.

To eliminate any subjectivity and ensure total transparency, we have fundamentally reconstructed the classification methodology in the revised manuscript. As detailed in the extensively revised Section 3.2, the classification is now entirely driven by quantitative physical metrics and statistically validated:

(1) Quantitative topological clustering (Text S2): Instead of subjective grouping, the 20 identified specific L-J weather types were aggregated into four major archetypes strictly based on their shared physical topology. We have added a new section (Text S2) in the Supplementary Material that explicitly lists the definitive, quantitative criteria used for this clustering: specifically relying on the polarity of SLP anomalies, the sign of geostrophic vorticity, and the primary azimuth of the geostrophic wind vectors. This ensures the classification rule is completely objective, transparent, and reproducible.

(2) Statistical validation via ANOVA (Fig. 6 & Table S2): To quantitatively prove that these four clustered archetypes are not arbitrary but represent fundamentally distinct atmospheric environments, we performed a One-Way Analysis of Variance (ANOVA). As explicitly added in Section 3.2, we calculated the nocturnal anomalies (Δ) of key micro-meteorological variables (T, RH, WS, PBLH, and U^*) across the four groups. The ANOVA results (all $p < 0.01$) provide definitive statistical proof that our classification algorithm objectively isolates completely different boundary layer thermodynamic structures.

(3) Direct evidence of high-altitude consistency (Fig. S5): Furthermore, to prove that this surface-based classification effectively captures broader synoptic forcing, we generated a new figure (Fig. S5). This explicitly demonstrates that the SLP gradients governing our categories perfectly align with the 850 hPa geostrophic wind flows across all identified types.

Lines 259-263:

Furthermore, to explicitly validate that this SLP-based classification accurately captures airflow characteristics in lower troposphere, Fig. S5 illustrates the spatial distributions of mean SLP overlaid with 850 hPa wind fields for the 20 identified weather types. The spatial patterns demonstrate a high degree of physical consistency, wherein the surface pressure gradients align with the 850 hPa wind field. This confirms that the SLP-based Lamb-Jenkinson method is highly robust and effectively represents synoptic circulation background of upper boundary-layer.

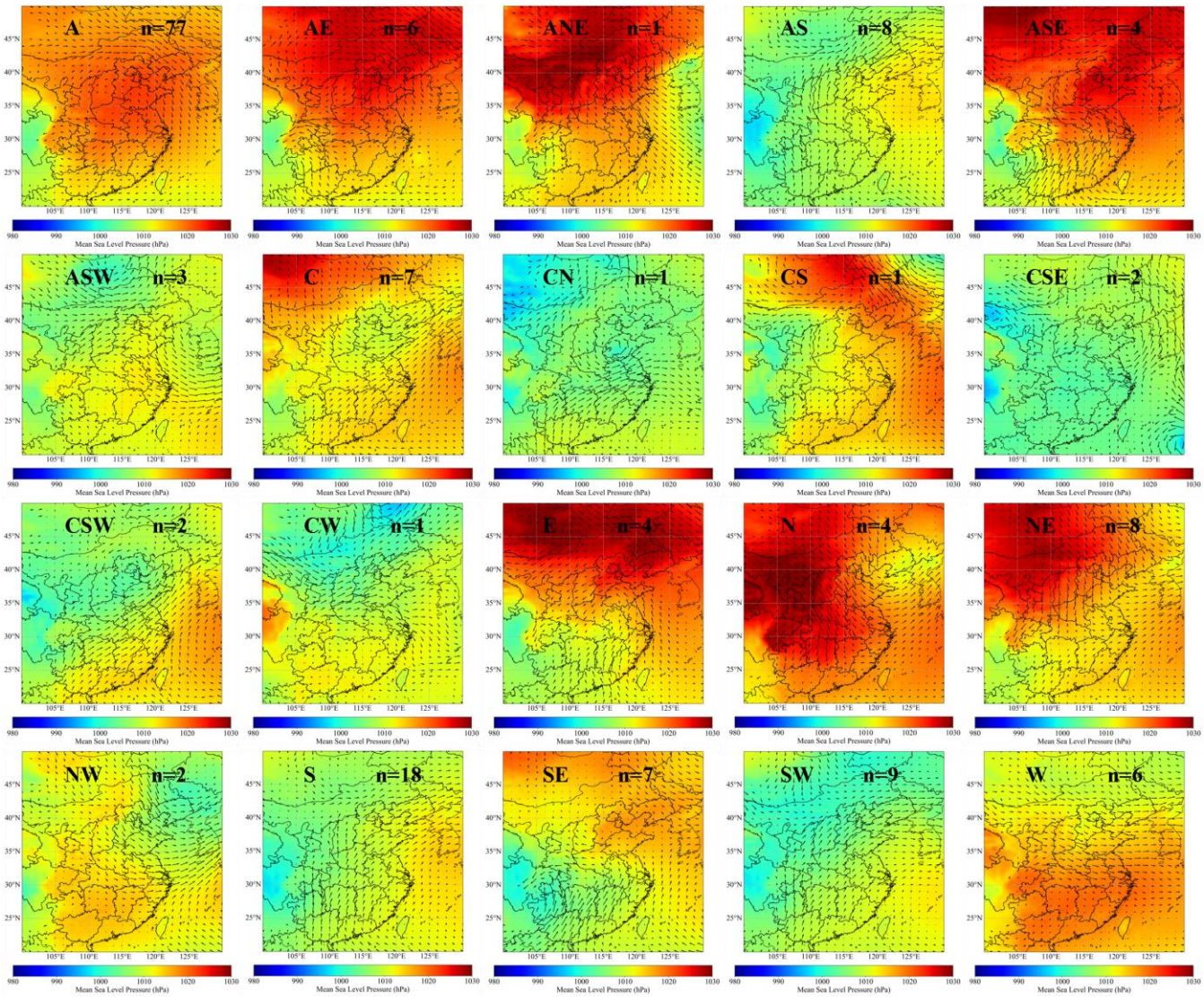


Figure S5: Spatial distribution of composite mean SLP and 850 hPa wind fields under different weather types (Preliminarily identified based on the Lamb-Jenkinson synoptic circulation classification method; n denotes the number of days).

Lines 276-296:

Notably, to extract the overarching dynamical mechanisms and reduce the statistical noise of the 20 specific Lamb-Jenkinson weather types, we quantitatively clustered them into four major archetypes: Anticyclonic (A-type), Cyclonic (C-type), Southerly (S-type), and West-North-East (WNE-type). Rather than subjective grouping, this clustering was rigorously based on their shared physical topology: specifically, the polarity of SLP anomalies, geostrophic vorticity, and the primary azimuth of geostrophic wind vectors. The detailed quantitative criteria for each of the four weather types are provided in Text S2. To further validate the physical distinctness of this

categorization, composite analysis of the synoptic fields and Analysis of Variance (ANOVA) on localized boundary layer variables were conducted.

To verify that the four grouped weather types possess fundamentally distinct atmospheric backgrounds, we analyzed their composite mean SLP and 850 hPa wind fields (Fig. 5). The spatial distributions unequivocally demonstrate distinct synoptic forcings: A-type is dominated by a strong, uniform high-pressure center over the study region (Fig. 5(a)); C-type is characterized by cyclonic curvature and low-pressure system (Fig. 5(b)); S-type is driven by intense southerly advection between a western low and an eastern high (Fig. 5(c)); and WNE-type features strong northeasterly flows driven by a massive continental high to the northwest (Fig. 5(d)). Furthermore, to statistically confirm that these different synoptic structures translate into distinctly different local thermodynamic environments, a One-Way ANOVA was performed on the nocturnal anomalies of key meteorological variables (T, RH, WS, PBLH and U^*) across the four groups. The resulting statistical distributions and data spreads are visually compared in Fig. 6, while the precise quantitative parameters and significance test results are detailed in Table S2. To strictly isolate the meteorological perturbations driven by synoptic systems and to eliminate the influence of seasonal and interannual backgrounds, the nocturnal anomalies (Δ) for key meteorological variables were calculated as the difference between the NOI days' specific nocturnal average and the corresponding monthly nocturnal mean. The results show that the inter-group differences are highly statistically significant (all $p < 0.01$), definitively proving that our quantitative classification objectively separates fundamentally different boundary layer environments.

Text S2: Quantitative grouping criteria.

(1) A-type (Anticyclonic group): This category quantitatively lumps all subtypes characterized by strong anticyclonic vorticity and positive SLP anomalies dominating the North China Plain (e.g., Pure A, and hybrid A types like AE, AW). Physically, these are unified by their shared capacity to induce broad regional subsidence.

(2) C-type (Cyclonic group): This lumps subtypes dominated by cyclonic vorticity and negative SLP anomalies (e.g., Pure C, and hybrid C types), unifying them through their shared dynamic triggering of localized convective downdrafts or atmospheric instability.

(3) S-type (Southerly group) & WNE-type (West-North-East group): The directional types

were categorized quantitatively based on the dominant azimuth of the geostrophic wind vectors and the strong orientation of the pressure gradient force, representing distinct horizontal advection and shear-induced mixing profiles.

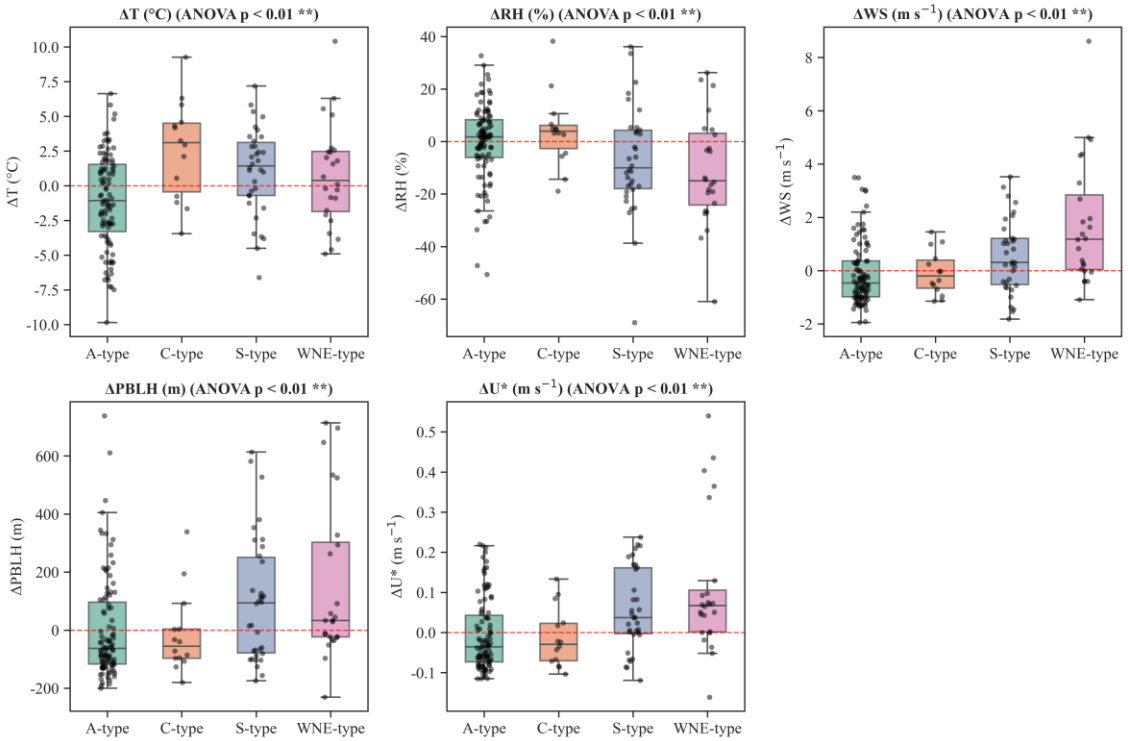


Figure 6: One-way ANOVA results for key meteorological variables (T, RH, WS, PBLH and U^*) of different synoptic categories. In each boxplot, the central black solid line indicates the median. The horizontal red dashed line denotes the zero-anomaly reference.

Table S2. Statistical summary of nocturnal meteorological anomalies and ANOVA results under the four weather types.

Variable	A-type	C-type	S-type	WNE-type	p-value
ΔT (°C)	-1.07 ± 3.41	2.60 ± 3.54	1.06 ± 3.18	0.77 ± 3.70	$< 0.01^{**}$
ΔRH (%)	-0.31 ± 14.82	4.08 ± 14.00	-7.12 ± 20.46	-11.15 ± 20.72	$< 0.01^{**}$
ΔWS (m s^{-1})	-0.10 ± 1.21	-0.08 ± 0.83	0.54 ± 1.39	1.74 ± 2.32	$< 0.01^{**}$
ΔPBLH (m)	3.56 ± 178.15	-14.44 ± 139.19	102.41 ± 216.82	156.22 ± 274.82	$< 0.01^{**}$
ΔU^* (m s^{-1})	-0.01 ± 0.09	-0.01 ± 0.07	0.06 ± 0.10	0.11 ± 0.17	$< 0.01^{**}$

Note: Data are presented as Mean ± Standard Deviation. The anomalies (Δ) were calculated relative to their respective monthly nocturnal means. The p-values are derived from One-Way ANOVA tests indicating statistical significance under the four weather types.

5. The measurement stations are not described. When presenting NOI statistics by station, the surrounding environment of each site is essential context. If a station is located near NO_x sources, the ozone signal will be titrated, and any observed increase will be attenuated or masked. Without characterizing the local emission environment, it is impossible to assess whether the detected NOIs are genuinely representative of mesoscale transport or simply artefacts of local source variability from the preceding hours.

Response 5: Thanks for reviewer's comments. To clarify the representativeness of our stations, we have detailed the environmental context of the measurement sites in the revised manuscript (Section 2.1). We respectfully provide the following two robust justifications to confirm that the observed NOI represent synoptic forcing:

(1) The nature of urban stations (Section 2.1): We clarified in the revised manuscript that all four measurement sites (KF, DY, XY, DX) are officially classified as national "urban evaluation sites" (which serve as urban stations) located within the built-up areas of Xinxiang. According to national siting criteria, these stations are specifically positioned to avoid direct, isolated micro-scale point sources (e.g., immediate traffic arteries or industrial facilities). Consequently, they share a consistent urban typology and experience comparable baseline NO titration sinks. This consistency minimizes the risk of severe, localized titration artifacts masking the regional signal.

(2) The rigorous simultaneous occurrence filter (Section 2.3): More importantly, as stated in Section 2.3, to completely rule out the possibility that the detected events are artefacts of local source variability, our study strictly filtered and focused only on representative NOI days where the O_3 surge occurred simultaneously across all different stations. A highly localized emission anomaly or a sudden drop in local NO_x at one specific street corner cannot physically trigger an identical, simultaneous O_3 surge across four geographically separated stations. These simultaneous occurrences serve as undeniable evidence of synoptic forcing (such as boundary-layer subsidence or regional advection).

Lines 91-99:

It is important to note that all four stations are officially classified as urban evaluation sites located within the urban areas of Xinxiang. In this study, these four stations were deliberately selected due to their strong spatial representativeness over the urban core and their high data completeness. Because these stations share a consistent urban typology, they experience highly

comparable baseline chemical environments (e.g., similar baseline nitrogen monoxide (NO) titration sinks and anthropogenic precursor availability). This spatial consistency is a crucial methodological design: it effectively minimizes random micro-scale chemical biases and isolated emission noise. By strictly controlling for these localized chemical heterogeneities, we ensure that the concurrent NOI events captured by this network genuinely reflect the overarching regional synoptic forcing and its subsequent, synchronized mechanical disruption of the local boundary layer, rather than random chemical artifacts.

Lines 234-242:

It is worth noting that non-overlapping NOI events frequently occur among the different stations, highlighting the inevitable influence of random localized emission noise and uncoordinated micro-environmental fluctuations. To rigorously isolate the overarching synoptic-scale meteorological drivers from these random local chemical/emission noises, this study specifically focused on representative events where NOI occurred simultaneously across all stations. Rather than dismissing local boundary-layer processes, these simultaneous occurrences serve as robust indicators of powerful regional episodes. They demonstrate that the large-scale synoptic forcing was sufficiently intense to synchronize the local boundary-layer dynamics (e.g., vertical wind shear and turbulent mixing) across the entire urban region. This rigorous screening ensures that the localized physical mechanisms evaluated in subsequent sections are systematically driven by macro-weather types, rather than coincidental local perturbations.

6. The rationale for selecting 850 hPa in Figure 3 is not provided in the methodology, and the wind scale is missing from the figure.

Response 6: Thanks for reviewer's comments. We have addressed both points in the revised manuscript:

(1) Rationale for 850 hPa: We have added an explicit justification to the Methodology section (Section 2.1). The revised text now explains: "Notably, the 850 hPa pressure level (approximately 1500 m above ground level) was specifically selected for the spatial wind field analysis. Because this altitude generally resides just above the planetary boundary layer, the airflow is largely free from localized surface friction and complex topographic disturbances. Consequently, it serves as the

most representative level for identifying mesoscale horizontal advection, low-level jets, and regional synoptic transport pathways that drive O_3 redistribution."

(2) Missing wind scale: We have now updated the figures (e.g., Fig. 7) to include a standard reference wind vector scale (→ 10 m s^{-1}) in each panel to accurately quantify the geostrophic wind arrows, alongside the existing color bar for absolute wind speed.

Lines 110-114:

Notably, the 850 hPa pressure level (approximately 1500 m above ground level) was specifically selected for the spatial wind field analysis. Because this altitude generally resides just above the planetary boundary layer, the airflow is largely free from localized surface friction and complex topographic disturbances. Consequently, it serves as the most representative level for identifying mesoscale horizontal advection, low-level jets, and regional synoptic transport pathways that drive O_3 redistribution.

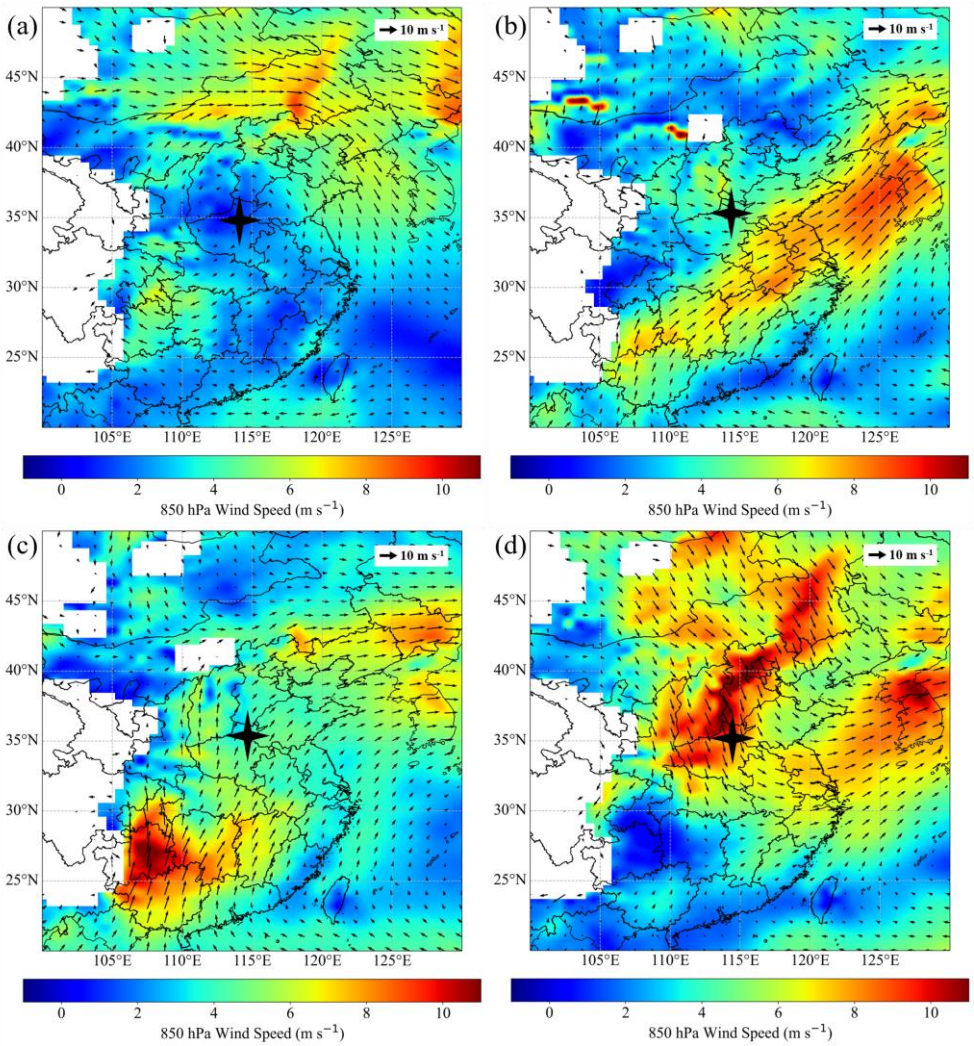


Figure 7: Spatial distribution of wind field at 850hPa under different weather types: (a) A-type, (b) C-type, (c) S-type, (d) WNE-type (asterisk indicates the location of Xinxiang).

7. Vertical profile data sources are not identified. When vertical profiles are discussed, no information is given about the data origin. The wind legend in Figure 5 is also incomplete.

Response 7: Thanks for reviewer's comments. We have revised relevant text in manuscript:

(1) Vertical profile data sources: The specific data origin and resolution for the vertical profiles were detailed in the Methodology (Section 2.1), where we stated that the "17-layer vertical profiles (500-1000 hPa)... were acquired from the Modern-Era Retrospective Analysis for Research and Applications dataset (MERRA-2)."

(2) Incomplete wind legend: This figure (revised Fig. 10) mainly illustrates vertical airflow characteristics (upward and downward motions) over Xinxiang. The sign of vertical pressure velocity directly indicates airflow direction: positive values represent downward motion, while negative values correspond to upward motion. Accordingly, we have removed the redundant wind vector arrows from the figure.

Lines 99-103:

Sea level pressure (SLP) data and 17-layer vertical profiles (500-1000 hPa) of vorticity, wind speed (WS), wind direction, temperature (T), relative humidity (RH) and O_3 concentration were acquired from the Modern-Era Retrospective Analysis for Research and Applications dataset (MERRA-2, Version 2, with a spatial resolution of 0.5° × 0.625° and temporal resolutions of 1 hour for surface data and 3 hours for 3D vertical profiles) (https://disc.gsfc.nasa.gov/).

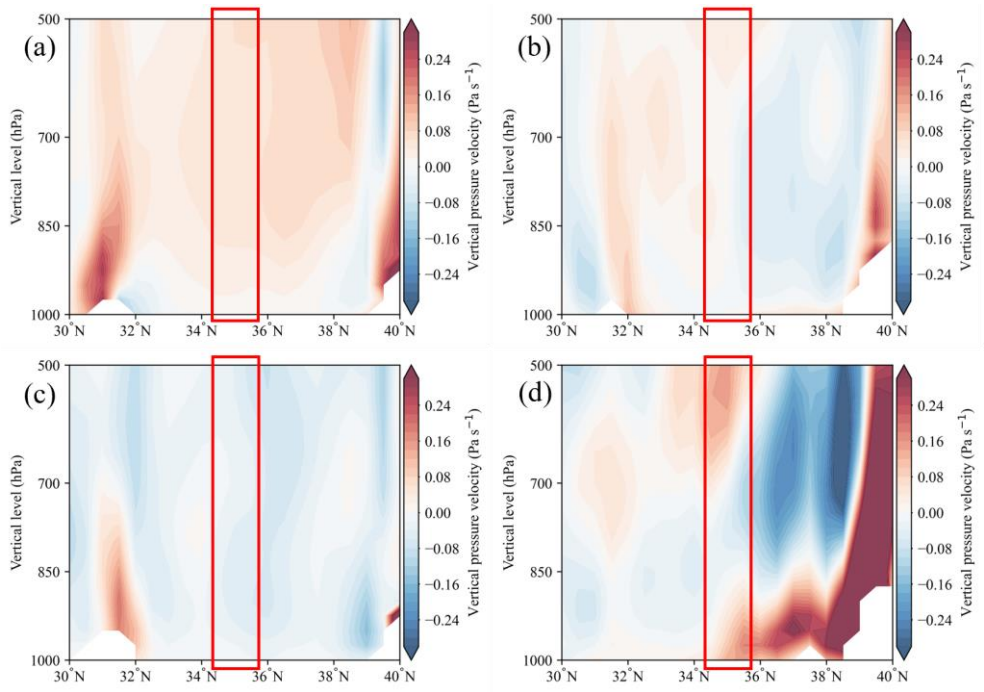


Figure 10: Vertical profiles of pressure velocity under different weather types: (a) A-type, (b) C-type, (c) S-type, (d) WNE-type (red rectangles indicate the region of Xinxiang). In terms of vertical pressure velocity, negative values correspond to upward motion, while positive values indicate subsidence.

Results and Interpretation:

1. The finding that most NOI events occur between March and September adds no new knowledge. This is simply when background ozone concentrations are highest, and the result follows trivially from that fact.

Response 1: Thanks for reviewer's comments. March to September is indeed the period with the highest background O_3 concentrations due to intense daytime photochemistry. At first glance, the seasonality of NOI does appear to perfectly mirror this background trend.

This phenomenon made us realize a flaw in our original narrative: we failed to clearly articulate the fundamental physical distinction between a passive photochemical background and an active dynamic intrusion. Inspired by reviewer's comment, we have introduced a "Reservoir vs. Trigger" paradigm in the revised manuscript to explicitly demonstrate why this seasonal finding is far from trivial:

(1) The reservoir (high background): The warm season builds up a large O_3 reservoir aloft. Within the nocturnal boundary layer, intense NO titration occurs. Even with extremely high

daytime O_3 levels, surface O_3 concentration declines rapidly at night. By contrast, O_3 in the residual layer is barely affected by titration and thus maintains high concentrations persistently.

(2) The trigger (active physical forcing): At night, O_3 cannot be produced via photochemical reactions, so its concentration rise is solely driven by physical transport. Although the residual layer holds abundant O_3 reservoirs in the warm season, the high-concentration O_3 can reach the surface and trigger NOI events when strong meteorological mechanical triggers (e.g., intense wind shear and prominent anticyclonic subsidence) break through the inversion layer and drive downward transport. Furthermore, strong NO titration occurs near the surface at night. The emergence of NOI also requires overcoming O_3 loss caused by titration to achieve a net increase in O_3 concentration.

(3) Clarifications in the revised text: To dispel the potential misconception that NOI is a passive byproduct of high backgrounds, we have expanded Section 3.1.1. We explicitly state: "While the warm season provides a highly concentrated aloft reservoir, the actual occurrence of an NOI event (which must vigorously overpower the intense local nocturnal NO titration) strictly requires the concurrent presence of specific dynamic meteorological triggers."

By explicitly separating the photochemical availability of the reservoir from the meteorological triggers (the core focus of this study), we believe the non-trivial nature and scientific value of these dynamic transport events are now robustly established.

Lines 194-197:

However, it is crucial to emphasize that a high regional O_3 background does not trivially dictate the occurrence of NOI. While the warm season provides a highly concentrated aloft reservoir, the actual occurrence of an NOI event (which must vigorously overpower the intense local nocturnal NO titration typical of urban environments) strictly requires the concurrent presence of specific dynamic meteorological triggers.

2. The role of calm conditions versus high wind speeds is not sufficiently interrogated. While the results suggest a higher frequency of NOI under calm conditions, events are also identified under elevated wind speeds. These cases could reflect fumigation from elevated layers, or transport associated with pre-frontal air masses carrying accumulated pollution that is subsequently scavenged after frontal passage — a mechanism already documented in the literature. This alternative explanation is not discussed.

Response 2: Thanks for reviewer's comments. We have completely rewritten Section 3.3 in the revised manuscript to shift the focus from descriptive seasonal meteorology to rigorous boundary-layer mechanical forcing. Following reviewer's expert suggestion, the revised text now rigorously contrasts these scenarios:

(1) Interrogating calm conditions (A-type): We now explicitly characterize A-type as pure synoptic subsidence occurring under extremely calm conditions. As added to the revised text, the negative anomalies in local wind speed and friction velocity confirm a highly stable environment. Here, the trigger is macro-scale subsidence pushing against the inversion.

(2) Interrogating elevated wind speeds (WNE-type): Under WNE-type, we found high wind speeds (mean: $\Delta WS = 1.74$ m s^{-1}) and intense turbulent mixing (mean: $\Delta U^* = 0.11$ m s^{-1}). In the revised text, we have explicitly linked this observed intense mechanical downward mixing with the nocturnal "fumigation-like processes" documented in the literature.

Lines 323-329:

Under A-type, Xinxiang was located near a high-pressure center, with an outward-rotating wind field at 850 hPa (Figs. 5(a) and 7(a)), indicating the presence of an anticyclonic high-pressure system. Driven by this synoptic forcing, Xinxiang experienced extremely calm conditions. As explicitly demonstrated by the nocturnal anomalies in Fig. 6 and Table S2, A-type was characterized by negative anomalies in wind speed (mean: $\Delta WS = -0.10$ m s^{-1}) and friction velocity (mean: $\Delta U^* = -0.01$ m s^{-1}), alongside a strongly constrained boundary layer (mean: $\Delta PBLH = 3.56$ m, representing negligible expansion). This indicates that the overriding high-pressure system creates a highly stable environment. The explicit intrusion process of O_3 under this subsidence will be further verified in Section 3.4.

Lines 351-367:

Although Xinxiang often featured a massive continental high-pressure system (e.g., the Siberian High) to the northwest under WNE-type (Fig. 5(d)), their local dynamics are fundamentally different from the pure subsidence of A-type. At 850 hPa, the region was obviously influenced by a northwestern airflow (Fig. 7(d)), consistent with the geostrophic wind characteristics of WNE-type. Unlike A-type, where the study area sits calmly at the high-pressure center, under WNE-type, Xinxiang was located at the densely packed periphery of the advancing

high. Consequently, the macroscopic forcing shifts to intense horizontal pressure gradients (Figs. 5(d) and 7(d)). This kinematic distinction is perfectly captured by the localized surface anomalies (Table S2). WNE-type exhibited the most extreme positive anomalies among all categories, with local wind speed (mean: ΔWS = 1.74 m s^{-1}) and friction velocity (mean: ΔU^* = 0.11 m s^{-1}) far exceeding other types. Driven by this intense horizontal advection and wind shear, the nocturnal boundary layer experienced massive mechanical lifting (mean: $\Delta PBLH$ = 156.22 m). Furthermore, this intense mechanical mixing effectively breaks the nocturnal surface inversion, bringing slightly warmer air from aloft downward (detailed mechanism analysis is presented in Section 3.4.2). This vigorous downward mixing of the elevated residual layer shares conceptual similarities with the nocturnal fumigation-like processes documented in other literature (Wu et al., 2023; He et al., 2022), which also explains the observed positive temperature anomaly (mean: ΔT = 0.77 °C). Therefore, despite the high-pressure background, it is this extraordinarily strong localized shear and turbulent mixing, that serves as the primary mechanical driver forcing O_3 downward to the surface during WNE-type. Combined with rapid dispersion of local NO emissions under high winds that greatly mitigates nighttime titration, vigorous vertical entrainment counteracts both horizontal diffusion and titration loss of O_3, and ultimately causes a net O_3 surge.

3. The WNW weather type results are likely of limited ozone relevance. High wind speeds under this type are typically associated with enhanced dispersion, making it doubtful that these events represent meaningful ozone loading.

Response 3: Thanks for reviewer's comments. High wind speeds generally act as a diluting agent, which typically reduces the surface loading of primary pollutants (e.g., NO_x or CO). Under normal daytime conditions, this logic perfectly applies to O_3 as well.

Inspired by reviewer's comment, we recognized that our original manuscript failed to elaborate the physical effects of unique strong wind events within the nocturnal boundary layer. For nighttime O_3, strong winds associated with the WNE circulation pattern activate a coupled physical and chemical mechanism:

(1) Dispersion of the chemical sink (rather than the O_3 source): At night, O_3 in the urban surface layer is rapidly consumed via intensive NO titration, whereas abundant O_3 accumulates within the elevated residual layer aloft. Accordingly, near-surface strong winds exert far weaker

dilution effects on the scarce surface O_3 than they do during daytime. Meanwhile, such strong winds swiftly transport and dilute high-concentration local primary pollutants at night, mainly nitric oxide (NO). The rapid dilution of NO greatly weakens the dominant chemical sink for nocturnal O_3.

(2) Intense mechanical downward entrainment: Concurrently, these high wind speeds generate powerful localized mechanical turbulence. As explicitly validated by our localized anomalies (detailed in the revised Section 3.3), the WNE-type triggers massive mechanical lifting of the boundary layer (mean: ΔPBLH = 156.22 m) and generates extremely high friction velocity (ΔU^* = 0.11 m s^{-1}). The powerful turbulence mixing entrains the O_3-rich air from the residual layer downward to the surface.

Relevant revised text in the manuscript is presented in Lines 351–367.

4. Line 249 mentions a thermal low-pressure system without discussing its potential influence on ozone dynamics, which is a notable omission given the likely relevance of this feature to the observed transport patterns.

Response 4: Thanks for reviewer's comments. Thermal low-pressure systems are highly relevant to regional O_3 dynamics, particularly regarding daytime accumulation and large-scale mass transport.

In the original manuscript, we briefly mentioned this daytime thermal low-pressure system merely in the context of general seasonal climatology. However, we realized that introducing a daytime thermal feature without rigorously linking it to the specific nocturnal intrusion mechanism created a disjointed narrative.

Because the core focus of this study is the dynamic triggering of nocturnal O_3 enhancements (NOI), the daytime thermal low-pressure system (while crucial for building the aloft O_3 reservoir) is not the direct mechanical driver that physically breaks the nocturnal surface inversion. Therefore, to resolve this omission and prevent any distraction from the core causal mechanisms, we took the following steps:

(1) Removal of disjointed daytime climatology: As part of our major structural overhaul of Section 3.3 (to refocus the manuscript strictly on nocturnal mechanical triggers), we have completely removed the descriptive paragraph regarding daytime seasonal climatology, including the isolated reference to the thermal low-pressure system.

(2) Exclusive focus on nocturnal transport drivers: Instead, the revised discussion of the S-type

transport pattern now focuses exclusively on the definitive nocturnal synoptic and boundary-layer drivers. Specifically, we now comprehensively discuss the nocturnal tight pressure gradients and their specific localized mechanical responses: significant positive anomalies in local wind speed (mean: $\Delta WS = 0.54$ m s^{-1}) and friction velocity (mean: $\Delta U^* = 0.06$ m s^{-1}), which lead to substantial nocturnal boundary layer lifting (mean: $\Delta PBLH = 102.41$ m).

We believe that by completely removing the disconnected daytime climatology and focusing entirely on these rigorous nocturnal mechanical metrics, the revised manuscript now provides a highly focused, dynamically sound interpretation of the S-type nocturnal transport patterns.

Lines 342-350:

S-type represents a dynamic environment driven by distinct horizontal advection. Under S-type, Xinxiang was situated in a tight pressure gradient, typically between a western low and an eastern high (Figs. 5(c) and 7(c)). Driven by this synoptic setup, continuous southerly geostrophic winds prevailed over the region. As detailed in Table S2, S-type produced significant positive anomalies in local wind speed (mean: $\Delta WS = 0.54$ m s^{-1}) and friction velocity (mean: $\Delta U^* = 0.06$ m s^{-1}). These specific values rigorously demonstrate that beyond facilitating regional horizontal transport (which will be explicitly traced in Section 3.4.1), the southerly advection directly generates substantial localized mechanical turbulence at the surface, physically lifting the nocturnal boundary layer (mean: $\Delta PBLH = 102.41$ m). This localized mechanical shear serves as the direct trigger for breaking nocturnal stability, subsequently entraining O_3-rich air from the elevated residual layer down to the surface and triggering NOI events.

5. The decoupling of weather type frequencies, ozone concentrations, and Figure 3 meteorology makes it impossible to assess the actual severity of the identified increases. A summary table integrating these dimensions would greatly improve readability and analytical clarity. As currently presented, the results section is difficult to follow.

Response 5: Thanks for reviewer's comments. The original results section was difficult to follow and that the meteorological drivers felt disjointed from the severity of the events.

To fundamentally resolve this issue, we have completely overhauled the narrative in Section 3.3. However, regarding the specific construction of the summary table, we encountered a fundamental atmospheric chemistry caveat that led us to refine reviewer's suggestion:

(1) The risk of confounding dynamic severity with chemical mass balance: We initially attempted to construct the integrated table coupling weather types directly with specific absolute O_3 mass increments. However, we realized this approach inadvertently obscured the true physical mechanism. As is well established, the observed nocturnal O_3 increment is an extremely complex mass-balance outcome (involving horizontal advection, vertical entrainment, and non-linear chemical titration by NO). Because the absolute O_3 surge is heavily confounded by the baseline daytime accumulation, directly coupling it with overarching weather types risks implying an oversimplified linear causality.

(2) Establishing Table S2 as the quantitative severity matrix: To maintain a strict scientific focus on the physical drivers while directly addressing a tabulated summary, we designated Table S2 (localized nocturnal meteorological anomalies) as our definitive diagnostic matrix. Instead of absolute chemical outcomes, Table S2 explicitly integrates and contrasts the intrinsic physical driving severity across all weather types (ΔWS, ΔU^*, ΔPBLH…). Since Figure 6 and Table S2 convey similar information, we place Figure 6 in the main text and Table S2 in the supplementary materials.

(3) Narrative coupling in the revised Section 3.3: Complementing Table S2, the narrative in the revised Section 3.3 is now strictly coupled. For each weather type, we immediately link the macro-scale synoptic forcing directly to these tabulated localized boundary-layer triggers (incorporating quantitative anomalies like T, RH, WS, U^* and PBLH).We believe that this mechanism-focused framework, anchored by Table S2 as the analytical benchmark, effectively resolves the readability issues and provides a clear integration of dimensions without oversimplifying the complex chemical mass balance of nocturnal O_3.

Relevant revised text in the manuscript is presented in Lines 307–367.

6. Supplementary figures are referenced repeatedly in the main text without adequate explanation.

Response 6: Thanks for reviewer's comments. To greatly improve the readability and ensure a smooth, self-contained narrative in the main text, we have conducted a comprehensive review of all supplementary citations and made the following major improvements in the revised manuscript:

(1) Expanding in-text interpretations: We have systematically gone through the manuscript and expanded the textual descriptions whenever a supplementary figure is cited. Instead of merely citing

the figure number, the revised main text now explicitly summarizes the key points and visual evidence provided by that specific supplementary figure, ensuring the reader understands the analytical point without strictly needing to open the supplementary file.

(2) Elevating critical data to the main text: Furthermore, we realized that some supplementary data were simply too critical to be left in the appendix. Accordingly, several key contents have been integrated into the main text.

Lines 213-214:

Therefore, we further analyzed the O_3 diurnal variations on NOI days categorized by their occurrence time across different seasons (Fig. 2).

Lines 231-233:

We established unified occurrence dates through cross-analysis of multi-station data (Fig. 3), and found that KF, XY, DX, and DY had 171 NOI days occurring on the same days during 2021-2023 in Xinxiang.

Lines 290-292:

The resulting statistical distributions and data spreads are visually compared in Fig. 6, while the precise quantitative parameters and significance test results are detailed in Table S2.

Lines 408-410:

To validate this process, we analyzed the vertical profiles of pressure velocity (Fig. 10), thermodynamic stability (Fig. S9), O_3 concentrations (Fig. S10), and surface turbulence metrics (Fig. 11).

7. The absence of summary tables makes the results section hard to navigate. Given the number of weather types and stations discussed, tabulated summaries are necessary.

Response 7: Thanks for reviewer's comments. To explicitly improve the navigation without introducing misleading causal attributions, we took the following comprehensive steps:

(1) Creating a highly standardized, predictable narrative pipeline (Sections 3.3, 3.4.1, and 3.4.2): Rather than relying on a simplified table, we fundamentally resolved the navigation issue by

completely overhauling the text to act as a structural table. We have standardized the narrative flow across Sections 3.3, 3.4.1, and 3.4.2. Now, for every single weather type, the reader is guided through an identical, highly predictable logical pipeline:

Triggering precondition: The macroscopic synoptic forcing.

3D origin: High-altitude regional backward trajectories proving the aloft reservoir.

Downward intrusion: Specific local vertical mixing metrics (e.g., CAPE, ΔU^*, and PBLH fluctuations) physically pulling the O_3 downward.

By stripping away disjointed seasonal climatology and adhering strictly to this identical, three-step causal framework for each weather type, the revised text allows readers to intuitively compare mechanisms across categories without getting lost.

(2) Optimizing the visibility and integration of existing diagnostic tables: We realized our original manuscript failed to effectively guide the reader to the existing summaries. We have now heavily integrated and signposted Table S1 (frequencies) and Table S2 (quantitative boundary-layer anomalies). By anchoring our standardized narrative much more smoothly to these comprehensive tables, the quantitative differences are now highly visible.

(3) Elevating critical data to the main text: We systematically reviewed the entire manuscript. To prevent the reader from constantly flipping between the main text and the supplement, we have elevated several critical pieces of information directly into the main manuscript, streamlining non-essential details into the appendices.

We believe these synergistic improvements (standardizing the narrative pipeline across Sections 3.3 and 3.4, alongside better leveraging robust existing tables) have drastically improved the analytical flow, making the Results section highly intuitive to navigate.

Relevant revised text in the manuscript is presented in Lines 307–451.

Conceptual and Terminological Issues:

1. Line 50: Discussing "formation mechanisms" in the context of nocturnal ozone is conceptually inconsistent. At night, photochemical ozone production is absent; the relevant process is titration by NO, not formation. The framing needs to be corrected.

Response 1: Thanks for reviewer's comments. In the strict context of atmospheric chemistry, the

word “formation” is intrinsically associated with photochemical production. Using it alongside nocturnal O_3 could indeed cause conceptual ambiguity and inadvertently mislead readers into thinking about chemical production.

To eliminate any potential for terminological confusion and to precisely reflect the true nature of these events, we have revised the manuscript and replaced “formation mechanisms” with “physical mechanisms”. The revised sentence in the introduction now reads: “While daytime O_3 pollution is well-documented, NOI remains poorly understood, necessitating the research into its meteorological drivers and physical mechanisms”.

Furthermore, to ensure absolute conceptual consistency throughout the entire manuscript and to highlight the physical nature of this research, we have systematically replaced “formation” with “physical mechanisms” or “physical transport” when discussing nocturnal events. We have even updated the title of the manuscript to reflect this precise mechanistic focus.

2. "Meteorological activities" (Line 49) is not standard scientific terminology and should be revised.

Response 2: Thanks for reviewer’s comments. Meteorological activities are not standard scientific terminology in this context. To ensure precise academic phrasing, we have revised the text and replaced it with “meteorological phenomena”. The revised sentence in the introduction now reads: “NOI events, usually driven by horizontal and vertical transport processes, are linked to meteorological phenomena such as sea-land winds (Nair et al., 2002), valley winds (Sánchez et al., 2005; Xue et al., 2023), low-level jets and convective storms (Zhu et al., 2020; Wu et al., 2023)”.

References

Bell, B., Hersbach, H., Simmons, A., Berrisford, P., Dahlgren, P., Horányi, A., Muñoz-Sabater, J., Nicolas, J., Radu, R., Schepers, D., Soci, C., Villaume, S., Bidlot, J. R., Haimberger, L., Woollen, J., Buontempo, C., and Thépaut, J. N.: The ERA5 global reanalysis: Preliminary extension to 1950, Q. J. R. Meteorolog. Soc., 147, 4186-4227, https://doi.org/10.1002/qj.4174, 2021.

Chen, X., Huang, B., Li, M., Xiao, R., Cai, M., Zhou, Z., Ma, S., Gao, W., and Zhou, Z.: A prediction index of the volatile organic compounds pollution conditions in a chemical industrial park based on atmospheric stability, Sci. Total Environ., 919, 170862, https://doi.org/10.1016/j.scitotenv.2024.170862, 2024.

Cheng, X., Yu, J., Chen, L., Sun, Y., Zhang, H., Gao, S., Kong, S., Zheng, H., and Wang, H.: Influence of pollution control measures on the reduction of black carbon in an urban site of megacity, Tianjin, China based on ground-monitored and MERRA-2 reanalysis data, Sci. Total Environ., 912, 169466, https://doi.org/10.1016/j.scitotenv.2023.169466, 2024.

Chowdhury, F. I., Arteaga, C., Alam, M. S., Alam, I., and Resco de Dios, V.: Drivers of nocturnal stomatal conductance in C3 and C4 plants, Sci. Total Environ., 814, 151952, https://doi.org/10.1016/j.scitotenv.2021.151952, 2022.

He, C., Lu, X., Wang, H., Wang, H., Li, Y., He, G., He, Y., Wang, Y., Zhang, Y., Liu, Y., Fan, Q., and Fan, S.: The unexpected high frequency of nocturnal surface ozone enhancement events over China: characteristics and mechanisms, Atmos. Chem. Phys., 22, 15243-15261, https://doi.org/10.5194/acp-22-15243-2022, 2022.

He, Y., Wang, H., Wang, H., Xu, X., Li, Y., and Fan, S.: Meteorology and topographic influences on nocturnal ozone increase during the summertime over Shaoguan, China, Atmos. Environ., 256, 118459, https://doi.org/10.1016/j.atmosenv.2021.118459, 2021.

Hersbach, H., Bell, B., Berrisford, P., Hirahara, S., Horányi, A., Muñoz-Sabater, J., Nicolas, J., Peubey, C., Radu, R., Schepers, D., Simmons, A., Soci, C., Abdalla, S., Abellan, X., Balsamo, G., Bechtold, P., Biavati, G., Bidlot, J., Bonavita, M., De Chiara, G., Dahlgren, P., Dee, D., Diamantakis, M., Dragani, R., Flemming, J., Forbes, R., Fuentes, M., Geer, A., Haimberger, L., Healy, S., Hogan, R. J., Hólm, E., Janisková, M., Keeley, S., Laloyaux, P., Lopez, P., Lupu, C., Radnoti, G., de Rosnay, P., Rozum, I., Vamborg, F., Villaume, S., and Thépaut, J. N.: The ERA5 global reanalysis, Q. J. R. Meteorolog. Soc., 146, 1999-2049, https://doi.org/10.1002/qj.3803, 2020.

Hoshika, Y., De Carlo, A., Baraldi, R., Neri, L., Carrari, E., Agathokleous, E., Zhang, L., Fares, S., and Paoletti, E.: Ozone-induced impairment of night-time stomatal closure in O_3-sensitive poplar clone is affected by nitrogen but not by phosphorus enrichment, Sci. Total Environ., 692, 713-722, https://doi.org/10.1016/j.scitotenv.2019.07.288, 2019.

Li, M., Zhang, Q., Zheng, B., Tong, D., Lei, Y., Liu, F., Hong, C., Kang, S., Yan, L., Zhang, Y., Bo, Y., Su, H., Cheng, Y., and He, K.: Persistent growth of anthropogenic non-methane volatile organic compound (NMVOC) emissions in China during 1990–2017: drivers, speciation and ozone formation potential, Atmos. Chem. Phys., 19, 8897-8913, https://doi.org/10.5194/acp-19-8897-2019, 2019.

Lu, X., Zhang, L., Chen, Y., Zhou, M., Zheng, B., Li, K., Liu, Y., Lin, J., Fu, T.-M., and Zhang, Q.: Exploring 2016–2017 surface ozone pollution over China: source contributions and meteorological influences, Atmos. Chem. Phys., 19, 8339-8361, https://doi.org/10.5194/acp-19-8339-2019, 2019.

Nair, P. R., Chand, D., Lal, S., Modh, K. S., Naja, M., Parameswaran, K., Ravindran, S., and Venkataramani, S.: Temporal variations in surface ozone at Thumba (8.6°N, 77°E)-a tropical coastal site in India, Atmos. Environ., 36, 603-610, https://doi.org/10.1016/S1352-2310(01)00527-1, 2002.

Sánchez, M. L., De Torre, B., García, M. A., and Pérez, I.: Ozone concentrations at a high altitude station in the Central Massif (Spain), Chemosphere, 60, 576-584, https://doi.org/10.1016/j.chemosphere.2004.12.079, 2005.

Shi, J., Wu, X., Han, X., Zhong, Y., Wang, Z., and Ning, P.: Characterization and sources of carbonaceous aerosols in southwest plateau of China: Effects of biomass burning and low oxygen concentration, Atmos. Environ., 318, 120250, https://doi.org/10.1016/j.atmosenv.2023.120250, 2024.

Stein, A. F., Draxler, R. R., Rolph, G. D., Stunder, B. J., Cohen, M. D., and Ngan, F.: NOAA's HYSPLIT atmospheric transport and dispersion modeling system, Bull. Am. Meteorol. Soc., 96, 2059-2077, https://doi.org/10.1175/BAMS-D-14-00110.1, 2015.

Wang, G., Liu, X., Kong, F., Zhu, Z., Yan, P., Gao, W., and Zhao, N.: Characteristics of fine particulate matter in Linyi during the 24th Olympic winter Games: An insight into the components, sources, transport pathways, and source distribution, Atmos. Pollut. Res., 15, 102034, https://doi.org/10.1016/j.apr.2023.102034, 2024.

Wang, H., Fan, L., Deng, X., Huang, H., and Ye, D.: Research on the characteristics and triggering factors of concurrent events of ozone pollution and nocturnal ozone increase in Xinxiang, China, Atmos. Environ., 361, 121494, https://doi.org/10.1016/j.atmosenv.2025.121494, 2025.

Wang, H., Wang, H., Lu, X., Lu, K., Zhang, L., Tham, Y. J., Shi, Z., Aikin, K., Fan, S., Brown, S. S., and Zhang, Y.: Increased night-time oxidation over China despite widespread decrease across the globe, Nat. Geosci., 16, 217-223, https://doi.org/10.1038/s41561-022-01122-x, 2023a.

Wang, K., Xie, F., Sulaymon, I. D., Gong, K., Li, N., Li, J., and Hu, J.: Understanding the nocturnal ozone increase in Nanjing, China: Insights from observations and numerical simulations, Sci. Total Environ., 859, 160211, https://doi.org/10.1016/j.scitotenv.2022.160211, 2023b.

Wu, Y., Chen, W., You, Y., Xie, Q., Jia, S., and Wang, X.: Quantitative impacts of vertical transport on the long-term trend of nocturnal ozone increase over the Pearl River Delta region during 2006–2019, Atmos. Chem. Phys., 23, 453-469, https://doi.org/10.5194/acp-23-453-2023, 2023.

Xue, Y., Wang, L., Jing, Y., Zhang, T., He, S., Ho, K. F., Huang, Y., Chen, L., Cui, L., and Cao, J.: Asian monsoon and local valley wind caused transport of volatile organic compounds episode across Qinling Mountain in China, J. Geophys. Res.: Atmos., 128, e2022JD038256, https://doi.org/10.1029/2022JD038256, 2023.

Zhu, L., Han, X., Xu, L., Guan, X., Gong, A., Liu, H., and Zhang, M.: Nocturnal ozone enhancement in Shandong Province, China, in 2020–2022: Spatiotemporal distribution and formation mechanisms, Sci. Total Environ., 925, 171542, https://doi.org/10.1016/j.scitotenv.2024.171542, 2024.

Zhu, X., Ma, Z., Li, Z., Wu, J., Guo, H., Yin, X., Ma, X., and Qiao, L.: Impacts of meteorological conditions on nocturnal surface ozone enhancement during the summertime in Beijing, Atmos. Environ., 225, 117368, https://doi.org/10.1016/j.atmosenv.2020.117368, 2020.